Mon. Not. R. Astron. Soc. **000**, 000–000 (0000) Printed 29 October 2014 (MN LATEX style file v2.2)

HIGHz: A Survey of the Most HI-Massive Galaxies at z ∼0.2

Barbara Catinella[1]⋆ and Luca Cortese[1]
[1]*Centre for Astrophysics & Supercomputing, Swinburne University of Technology, Hawthorn, VIC 3122, Australia*

arXiv:1410.7464v1 [astro-ph.GA] 28 Oct 2014

ABSTRACT
We present the results of the HIGHz Arecibo survey, which measured the HI content of 39 galaxies at redshift $z > 0.16$ selected from the Sloan Digital Sky Survey. These are all actively star-forming, disk-dominated systems in relatively isolated environments, with stellar and HI masses larger than 10^{10} $M_\odot$ and redshifts $0.17 \leq z \leq 0.25$. Our sample includes not only the highest-redshift detections of HI emission from individual galaxies to date, but also some of the most HI-massive systems known. Despite being exceptionally large, the HI reservoirs of these galaxies are consistent with what is expected from their ultraviolet and optical properties. This, and the fact that the galaxies lie on the baryonic Tully-Fisher relation, suggests that HIGHz systems are rare, scaled-up versions of local disk galaxies. We show that the most HI-massive galaxies discovered in the Arecibo Legacy Fast ALFA survey are the local analogues of HIGHz, and discuss the possible connection between our sample and the turbulent, gas-rich disks identified at $z \sim 1$. The HIGHz sample provides a first glimpse into the properties of the massive, HI-rich galaxies that will be detected at higher redshifts by the next-generation HI surveys with the Square Kilometer Array and its pathfinders.

Key words: galaxies: kinematics and dynamics – galaxies: evolution – galaxies: fundamental parameters – radio lines: galaxies

1 INTRODUCTION

In the past decade or so, studies of the cold atomic (HI) and molecular (H_2) hydrogen content of local galaxies have progressed from observations of relatively small samples to large surveys, including from several hundreds to a few tens of thousands objects (Barnes et al. 2001; Giovanelli et al. 2005; Catinella et al. 2010; Saintonge et al. 2011). This significant boost in number statistics, as well as in data quality, has made it possible to characterize the cold gas properties of galaxies from a statistical point of view, and to identify the most important scaling relations connecting gas and other galaxy properties in the local Universe (Catinella et al. 2010; Saintonge et al. 2011; Cortese et al. 2011; Huang et al. 2012; Boselli et al. 2014).

One of the main challenges for HI and H_2 astronomy is now to extend these investigations to cosmological distances, probing the variation of the cold gas content of galaxies with the age of the Universe. This is particularly important, as the remarkable decrease in the cosmic star formation rate density from $z \sim 1$ to 0 (*e.g.*, Lilly et al. 1996; Madau et al. 1996; Bell et al. 2005) must be a direct consequence of a change in the gas cycle of galaxies.

Thanks to the upgrade of the IRAM Plateau de Bure interferometer, observations of molecular hydrogen (as traced by the CO lines) have recently been able to reach redshifts that were unimaginable a decade ago, gradually revealing a population of exceptionally gas-rich ($M_{H_2}/M_\star \sim 1$), turbulent disk galaxies at z = 1-2 (Daddi et al. 2010; Genzel et al. 2011; Tacconi et al. 2013). Although only upcoming surveys with the Atacama Large Millimeter Array will determine whether or not these are representative of the star-forming galaxies at those redshifts, or just the gas-rich tail of the distribution, these pioneering observations confirm that the physical conditions of the interstellar medium have changed significantly in the last ∼8 billion years, and highlight the importance of the very gas-rich regime for galaxy evolution studies.

Unfortunately, HI astronomy lags behind in this respect. Due to sensitivity of current instruments, as well as man-made radio interference, HI observations are still struggling to detect the weak 21 cm emission beyond z ∼0.16 (Verheijen et al. 2007; Catinella et al. 2008; Jaffé et al. 2012; Fernández et al. 2013). Thus, spectral stacking of optically-selected samples that are undetected in HI surveys is currently the most powerful technique to measure the average HI content of galaxies at higher redshifts. Although not a substitute for HI detections, stacking has provided estimates of the cosmic HI density up to a redshift $z \sim 0.4$ (Lah et al. 2009). Only the next generation, deep HI surveys with the Square Kilometer Array (SKA, Carilli & Rawlings 2004) and its pathfinders, ASKAP (Johnston et al. 2008) and MeerKAT (Booth et al. 2009), will be able to detect HI emission at these and higher redshifts. As theoretical models predict a different evolution in the properties of the atomic and molecular gas phases (*e.g.* Obreschkow & Rawlings 2009; Lagos et al. 2011), quantifying how the HI reservoirs of galaxies vary with redshift is of primary importance.

Despite current constraints, carefully planned observations with existing radio telescopes can already peek into the z = 0.2 HI

⋆ bcatinella@swin.edu.au

© 0000 RAS

Table 1. Arecibo observing runs

Project ID	Dates	Redshift	SDSS selection	Allocation
A1803f	2003 Oct 8-18; Nov 8,10,22,23; Dec 6	0.09 – 0.18	DR1[a]	62h (18h @ $z > 0.16$)
A1803	2004 Mar 8-10,24-28; Apr 11-16,25	0.09 – 0.25	DR1[a],DR2[b]	121h (110h @ $z > 0.16$)
A2008	2005 Apr 19-26	0.16 – 0.25	DR3[c]	72h
A2270	2007 Mar 8-16	0.16 – 0.25	DR5[d]	80h
A2428	2011 May 3-15	0.16 – 0.32	DR7[e]	76h

[a]Abazajian et al. (2003); [b]Abazajian et al. (2004); [c]Abazajian et al. (2005); [d]Adelman-McCarthy et al. (2007); [e]Abazajian et al. (2009).

Universe, providing us with a glimpse of the gas-rich galaxy population that will be detected by the SKA pathfinders, and whose physical conditions might resemble those of higher redshift systems. Because of its exquisite sensitivity, the Arecibo radio telescope has a critical advantage for the detection of weak HI signals. With a collecting area that is equivalent to one-tenth of the full SKA, Arecibo can already detect HI emission at $z \sim 0.2$ with integrations of less than ten hours per object, as opposed to the few hundred hours necessary with current interferometers. Naturally, the downside of single-dish observations is their lack of spatial resolution, hence detecting HI emission at these redshifts is practically restricted to carefully selected galaxies in low density environments. However this drawback is partly compensated by the fact that gas-rich galaxies (which are the most likely to be detected) are preferentially found in isolation (Papastergis et al. 2013). Indeed, the feasibility of these observations was demonstrated by our pilot survey (Catinella et al. 2008).

In this paper we present the completed HIGHz survey, which measured the HI content of 39 optically-selected galaxies in the $0.17 < z < 0.25$ redshift interval. We describe our entire observing campaign and investigate the properties of the detected galaxies. In addition to the the highest redshift detection of HI emission from a galaxy to date ($z = 0.25$), this sample includes some of the most HI massive galaxies currently known. We discuss the relevance of HIGHz in the context of other surveys of exceptionally gas-rich galaxies, both in the local and in the higher redshift Universe.

All the distance-dependent quantities in this work are computed assuming $\Omega = 0.3$, $\Lambda = 0.7$ and $H_0 = 70$ km s^{-1} Mpc^{-1}. AB magnitudes are used throughout the paper.

2 SAMPLE SELECTION AND ARECIBO OBSERVATIONS

As mentioned in Catinella et al. (2008), where we presented our initial results, this programme started as a pilot survey to detect HI emission from disk galaxies at $z > 0.05$, *i.e.* beyond the redshift of past Arecibo surveys. We soon realized that the frequency interval corresponding to $0.11 < z < 0.16$ was inaccessible because of Radio Frequency Interference (RFI), therefore we concentrated our efforts on the $z > 0.16$ targets. By then, the first data release (Abazajian et al. 2003) of the Sloan Digital Sky Survey (SDSS; York et al. 2000) became available, which provided the ideal data base to search for galaxies with potentially large HI content, although the spectroscopic coverage of the sky area accessible to Arecibo was very limited.

The targets for HI spectroscopy were selected from the most recent SDSS spectroscopic data release available at the time of the observations (see Table 1) and according to the following criteria: (a) objects spectroscopically classified as galaxies; (b) observable from Arecibo during night-time (to minimize the impact of RFI and solar standing waves on our data); (c) redshift $0.16 < z < 0.27$. This interval corresponds to frequencies from 1120 to 1220 MHz and is set by a filter; (d) inclination $i \geq 45^\circ$ (computed from the axis ratio in *r*-band as in Catinella et al. 2010), for use in disk scaling relations. In the most recent run we relaxed this condition to include inclinations $i \geq 30^\circ$; (e) presence of Hα emission in the SDSS fiber, with line width between 100 and 700 km s^{-1} and equivalent width between 5 and 50 Angström (to avoid extreme star formation rates, usually associated to merger systems and/or starburst galaxies); (f) exponential disk profile, based on the likelihood of exponential versus DeVaucouleurs fit to the *r*-band profile (likelihood(exp)/likelihood(DeV)$> 10^6$).

After compiling the candidate list for each run, we discarded galaxies with redshifts corresponding to the frequency of known RFI, and/or in the vicinity of NVSS continuum sources that would cause ripples in the baselines. We then carefully inspected the SDSS image of each remaining galaxy, and excluded those with interacting or peculiar appearance, and/or with HI emission possibly contaminated by that of nearby objects. Specifically, we discarded targets with galaxies of similar size or luminosity lying within a 4′ radius (twice the the Arecibo beam). This was a crucial step in order to minimize the likelihood that our HI measurements are contaminated by companions with *potentially comparable HI content*, as the half power full width of the beam at the frequencies of our observations, ∼4′, subtends ∼800 kpc at $z = 0.2$. From the final list, we gave priority to the galaxies that looked more promising, *i.e.* those with largest apparent size and/or presence of spiral arms. Hence, although the parent sample out of which the targets were extracted is volume-limited and well defined, we deliberately picked our galaxies one by one, in order to maximize our chances of detecting HI emission. Not surprisingly, we obtained a sample that is strongly biased toward HI-massive objects. We targeted 49 galaxies with effective on-source integration times ranging between 52 and 260 minutes, and detected 39 objects. The 10 galaxies that were not detected have redshifts between 0.23 and 0.26 (except one with $z = 0.17$). A number of other potential targets were observed for a short time and abandoned because of various issues (too close to RFI, continuum sources, bad baselines).

The HI data were collected under four Arecibo programs and during several observing runs, which took place between Fall 2003 and Spring 2011. Table 1 lists the Arecibo program identifiers, the dates of the observations, the targeted redshift interval, the SDSS data release used for target selection, and the amount of telescope time allocated. The A1803 program was split into a Fall and a Spring portion (we indicate the former as A1803f), and was partly devoted to lower redshift observations. The A2428 program was accepted in 2008 but scheduled on the telescope three years later.

Including all the overheads, the total time spent on the $z > 0.16$ targets was 356 hours.

The observations were all carried out on site and in standard *position-switching* mode: each observation consisted of an *on/off* source pair, each integrated for 4 minutes (5 minutes in the last two observing runs), followed by the firing of a calibration noise diode. We used the L-band wide receiver, which operates in the frequency range 1120−1730 MHz, with a 1120−1220 MHz filter and a 750 MHz narrow-band (60 MHz) front-end filter to limit the impact of RFI on our observations. The interim correlator was used as a back-end, and the spectra were recorded every second with 9-level sampling. Two correlator boards, each configured for 12.5 MHz bandwidth, one polarization, and 2048 channels per spectrum (yielding a velocity resolution of 1.8 km s^{-1} at 1200 MHz before smoothing) were centered at or near the frequency corresponding to the SDSS redshift of the target. The Doppler correction for the motion of the Earth was applied during off-line processing. We note that, apart from the different redshift interval, the observing setup and data reduction pipeline are identical to those used for the GALEX Arecibo SDSS Survey (GASS; Catinella et al. 2010).

3 DATA REDUCTION

The data reduction was performed in the IDL environment using our own routines, which are based on the standard Arecibo data processing library developed by Phil Perillat. In summary, the data reduction of each polarization and *on-off* pair includes Hanning smoothing, bandpass subtraction, RFI excision, and flux calibration. Once the data are flux calibrated, a total spectrum is obtained for each of the two orthogonal linear polarizations by combining good quality records (those without serious RFI or standing waves). Each pair is weighted by a factor $1/rms^2$, where rms is the root mean square noise measured in the signal-free portion of the spectrum. The two polarizations are separately inspected and averaged, yielding the final spectrum.

After boxcar smoothing and baseline subtraction, the HI-line profiles are ready for the measurement of redshift, rotational velocity and integrated HI line flux. Recessional and rotational velocities are measured at the 50% peak level from linear fits to the edges of the HI profile. Our measurement technique is explained in more detail, *e.g.*, in Catinella, Haynes & Giovanelli (2007, §2.2).

Below we describe in more detail two very important steps of our data reduction, RFI excision and flux calibration.

3.1 RFI excision

The presence of RFI in our observations, which target a frequency interval that is well below the radioastronomy protected band (1400–1427 MHz), was the main challenge for our survey.

RFI can be generated both internally (by electrical equipment such as digital correlators and computers) and externally (*e.g.* by broadcasting radio and television stations, mobile phones, airport radars, and telecommunication satellites, but also by natural sources such as lightning). Single-dish radio telescopes are especially vulnerable to this problem because all incoming RFI, entering by scattering or reflection, enters the system coherently (Fridman & Baan 2001). Due to the variety of its possible sources, RFI spans a wide range of characteristics, both in the time and frequency domains; it can also be strongly polarized or completely unpolarized.

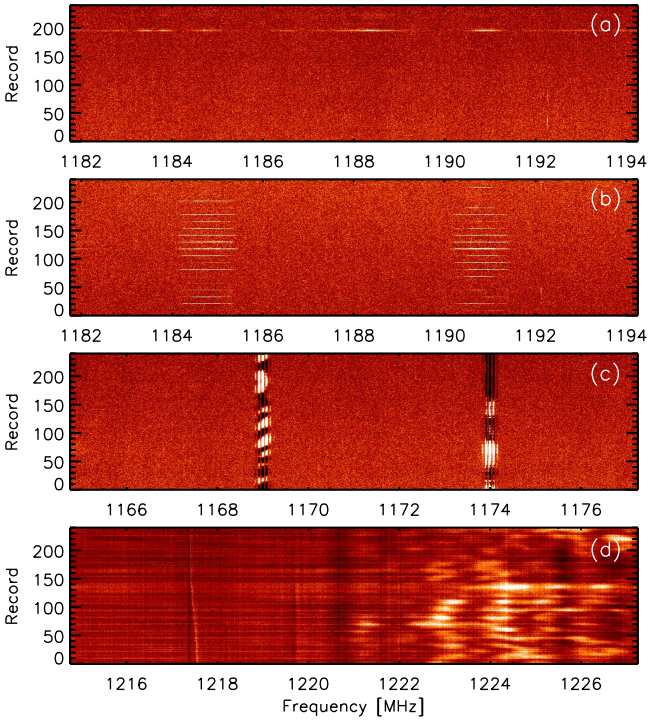

Figure 1. Examples of RFI affecting our data (from the A1803 run). Each panel shows the time-frequency representation of a processed on-off pair for the first correlator board. Spectra are recorded every second, thus the vertical scale can be read as time in seconds; the full 12.5 MHz bandwidth is shown on the horizontal axis. The top two panels illustrate examples of RFI that can be easily excised (see also Fig. 2). The RFI in (c) cannot be removed, but most of the frequency bandpass is still useful for the observations; (d) shows an observation that is completely compromised.

A few examples of the most common types of RFI that affected our observations are illustrated in Fig. 1. Each panel is the result of a processed 4 minute integration for the first correlator board (which shows one polarization only; the second board is almost identical unless the interference is strongly polarized); each row is a single spectrum, recorded every second. We always refer to frequency *channels* along the *x* axis and *records* along the *y* axis. In (a) the RFI appears for a very short time (a few seconds at most, around record 200), affecting all the bandpass; in (b) it is localized in the frequency domain (between 1184 and 1186 MHz, and between 1190 and 1192 MHz), but is present in several records. In both cases, the interference can be easily removed during data reduction by excising the affected records. These examples demonstrate the importance of a fast dump rate for spectrum recording, in order to minimize the amount of data that must be discarded because of RFI contamination. Panel (c) shows strong RFI signals at 1169 MHz and 1174 MHz; in this case the RFI cannot be simply removed by excising bad records, but the observation is not be compromised as long as the interference does not sit on top of the galaxy emission. Indeed, this example shows how critical an accurate knowledge of the galaxy redshifts was for this project, in order to anticipate at which frequencies the expected HI signal (which starts appearing only after many pairs have been co-added) would lie. Lastly, the presence of strong RFI outside the 12.5 MHz bandpass in (d) makes the data unusable. Our first observations immediately showed that the 1220–1230 MHz and 1270–1280 MHz frequency intervals were inaccessible due to type (d) RFI.

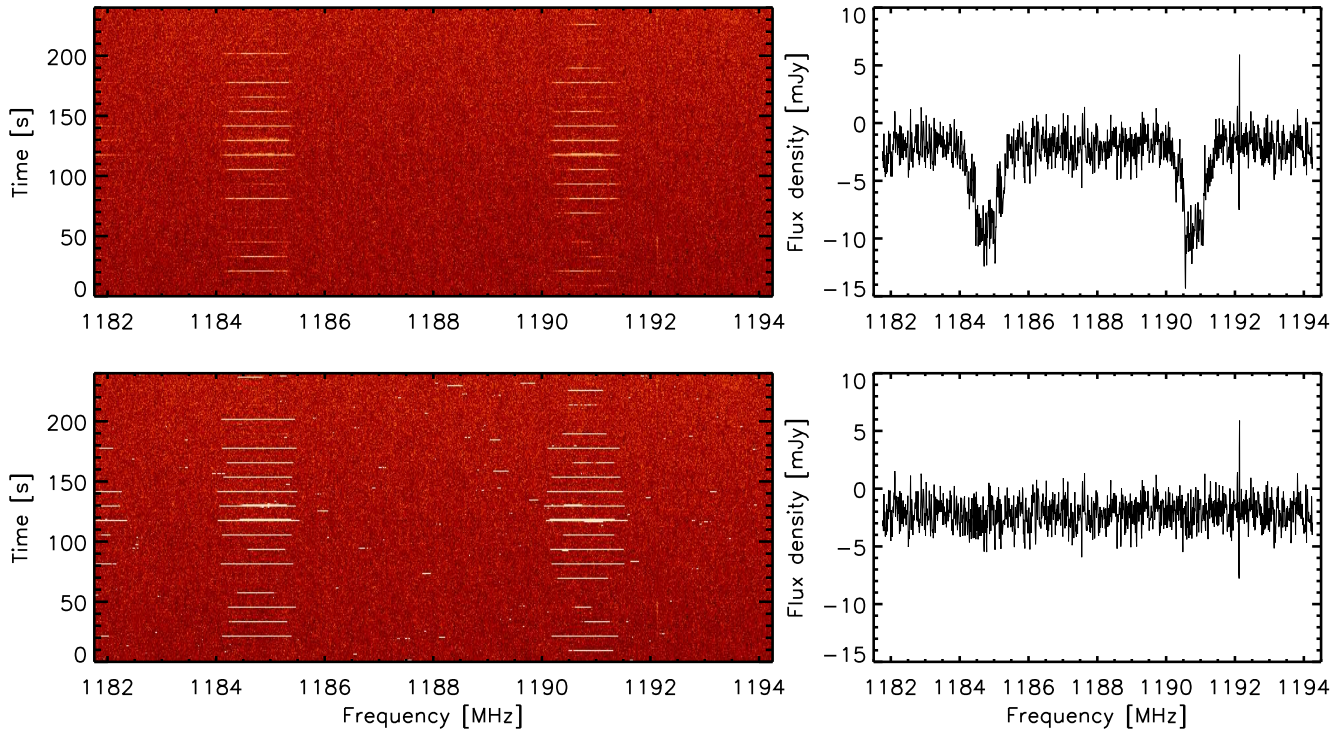

Figure 2. RFI excision. *Top:* Time-frequency representation of an observation of AGC 212887, showing strong RFI near 1185 and 1191 MHz (left), and corresponding spectrum (right). The RFI is in the off-source observation, thus it appears as absorption-like features in the spectrum. *Bottom:* The RFI mask is shown on top of the data (white pixels) on the left; the corresponding spectrum is RFI-free (right), except for a very narrow spike at 1192.1 MHz that is not identified by the RFI-masking algorithm.

Accurate planning of our observations was essential in order to minimize the impact of RFI on our data. As mentioned in Section 2, in addition to avoiding targets whose HI emission would lie in the proximity of known RFI of the type shown in Fig. 1c, we used front-end bandpass filters to restrict as much as possible the frequency interval "seen" by the correlator (to avoid RFI of the type of Fig. 1d).

Ideally, it would be convenient to rely on automatic algorithms to identify and remove RFI, but defining properties that distinguish RFI from astronomical signals is not a trivial task, especially in the presence of weak interference. Such algorithms are generally based on thresholding techniques, by which a portion of the data in the time and/or frequency domain is discarded when its mean (or some other statistical indicator) exceeds a certain value. A thorough testing is usually necessary to determine how to set the thresholds. Contrary to automatic algorithms, the human eye can easily identify RFI from the inspection of time-frequency representations such as those shown in Fig. 1 and thus, although impractical, manual excision achieves much better results. Because reliable RFI excision was extremely important for our survey, we resorted to an admittedly time-consuming, hybrid approach.

RFI excision is applied to the data before flux calibration, and its output is an RFI mask, which records the pixels in the time-frequency domain marked for rejection for each polarization and pair. The process includes the following steps:

(1) Processing each polarization of the *on-off* pair. Because we process the pairs first, RFI appears as an emission or absorption feature in the spectra depending on whether it is present/stronger in the *on* or in the *off* scan, respectively (see Fig. 2). This also implies that we discard data when RFI is present in at least one of the *on/off* scans.

(2) For each frequency channel, an *rms* noise spectrum across the time direction is computed, and an iterative linear fit performed, rejecting any points that deviate by 3σ or more from the fit. Fitting of the same channel is repeated until no more points are rejected, or an iteration limit is reached. Optionally, the data can be smoothed over N_{sm} frequency channels before searching for RFI. For our data set, we found that the best solution was to smooth by 0.3 MHz, and we did this by default.

(3) The rejected points are flagged, and time-frequency images for the two polarizations with the RFI mask overlaid (along with histograms showing the noise in each record) are displayed. This is illustrated in the bottom left panel of Fig. 2 for one polarization of one of our observations.

(4) At this point we inspect how well the automatic excision worked, and either run the program again or move to the next step. It is often necessary to run the program a few times with a different sigma threshold for pixel rejection and/or changing the number of channels N_{sm} for spectral smoothing in order to obtain the best result. RFI of the type seen in Fig. 1a usually requires to mask entire records, as many of the pixels in the affected records deviate by less than 3σ from the average noise. This is done by choosing a threshold r for record rejection (records with r per cent or more bad pixels are flagged).

(5) If necessary, we perform manual excision by selecting regions of the time-frequency image that should be rejected. The selected region is added to the RFI mask generated in point 4. Manual excision is usually needed for weak RFI that is not adequately

masked by the automatic algorithm, and for unusual RFI (*e.g.*, drifting in frequency).

(6) Lastly, the spectrum obtained after applying the RFI mask is shown (Fig. 2, bottom right). Here we can go back to (1) if needed, reject the pair if the data are unusable, or proceed to the flux calibration (the pair is reprocessed using the final RFI mask), keeping track of the number of records used at each frequency.

This algorithm is designed to identify strong RFI features in the time domain and spectrally broad RFI which is time-variable. RFI that is present in all records at a given frequency, such as that in Fig. 1c, is not masked. Fig. 2 shows an example of the application of our automatic RFI excision algorithm to our data, and the resulting HI spectrum before and after RFI masking (right panels).

3.2 Flux calibration

Standard position-switched observations of a source with Arecibo are followed by two measurements of a calibration diode, which is turned on for 10 seconds and then off for another 10 seconds, while the telescope points to the blank sky (the *off* galaxy position). The noise diode has a known temperature as a function of frequency for each polarization, hence processing its *on*/*off* observations allows one to determine the "system temperature", and convert correlator units into Kelvin degrees. The conversion to spectral flux density units is achieved by applying the gain curve, which provides the point source gain of the telescope in K/Jy for the specific receiver as a function of frequency and zenith angle of the observation. As discussed in van Zee et al. (1997); Springob et al. (2005) and most recently in Haynes et al. (2011, see their section 5.2), HI line flux densities derived from targeted single-dish observations in modern data sets are typically accurate to not better than 15%.

A technical problem made all the calibration scans taken between March 26 2004 and May 2005 unusable, thus we had to resort to a non-standard flux calibration for part of the A1803 and all the A2008 data. Because of a bug in the telescope control software (fixed in June 2005), selecting the 750 MHz narrow-band filter also silently triggered the "winking" calibration mode, which is used for pulsar observations. This caused our noise diode to be switched on and off with a frequency of 25 Hz (*i.e.*, every 40 ms), which had two effects: (a) render our calibration scans useless, and (b) inject extra noise in our observations, as the diode was on half of the time. This effectively increased the system temperature T_{sys} by ~15% (estimated from $0.5 \times T_{diode}/T_{sys} \sim 1.15$, where T_{diode} and T_{sys} are approximately 10 K and 33 K for our observations, respectively).

In order to calibrate these data, Phil Perillat at Arecibo kindly provided us with System Equivalent Flux Density (SEFD) curves for our receiver, which are obtained from a fit to the system temperature as a function of gain of the telescope. These fits give the point source SEFD of the telescope in Jy, as a function of frequency and zenith angle of the observation. We processed all the good calibration scans taken in 2003 and 2004, compared the diode calibration with the SEFD one, and found the two to be consistent within less than 10%. The SEFD curves are based on archival measurements of the system temperature taken under standard conditions, *i.e.* $T_{sys} \sim 33$ K at the frequencies of HIGHz. Hence, in order to account for the increased system temperature caused by the winking calibration, we multiplied the conversion factor obtained from the SEFD curves by 1.15. Conservatively, we consider the flux calibration of the galaxies affected by the winking calibration to have an additional uncertainty of 15% over the standard calibration, or a total uncertainty of ~21%. This problem affected partly or completely

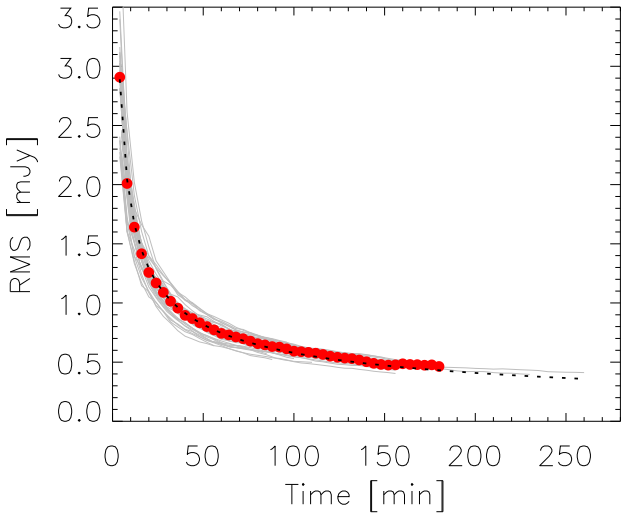

Figure 3. The *rms* noise is plotted versus on-source integration time, T_{int}, for individual galaxies (gray lines); red circles are running averages (computed when at least three data points were available). The *rms* decreases as $\sqrt{T_{int}}$ as expected (dotted line).

20 out of 39 galaxies, however the larger uncertainty in those HI fluxes does not affect our conclusions at all.

To our knowledge, these are the longest observations of individual galaxies done with Arecibo. As can be seen in Fig. 3, the measured *rms* noise of our observations computed from the unsmoothed HI spectra (*i.e.* at a velocity resolution of 1.8 km s^{-1} at 1200 MHz) decreases as the square root of the integration time, as expected.

4 DATA PRESENTATION

4.1 HI catalogue

The measured HI parameters for the 39 detected galaxies are listed in Table 2, ordered by increasing right ascension:
Col. (1): identification code in the Arecibo General Catalog (AGC, maintained by M.P. Haynes and R. Giovanelli at Cornell University).
Col. (2): SDSS identifier.
Col. (3): on-source integration time of the Arecibo observation, $T_{\rm on}$, in minutes. This number refers to *on scans* that were actually combined, and does not account for losses due to RFI excision (typically of order of a couple of percent). The fraction of usable data for our sample, *i.e.* the ratio between $T_{\rm on}$ and the total on-source time actually spent on each galaxy, varied between 50% and 100%, with an average of 84%. Pairs were discarded because of RFI that could not be excised or bad baselines.
Col. (4): velocity resolution of the final, smoothed spectrum in km s^{-1}.
Col. (5): redshift, z, measured from the HI spectrum. The error on the corresponding heliocentric velocity, cz, is half the error on the width, tabulated in the following column.
Col. (6): observed velocity width of the source line profile in km s^{-1}, W_{50}, measured at the 50% level of each peak. The error on the width is the sum in quadrature of the statistical and systematic uncertainties in km s^{-1} (the latter depend on the subjective choice of the HI signal boundaries and are usually negligible, see Catinella et al. 2010 for details).

Col. (7): velocity width corrected for instrumental broadening and cosmological redshift only, $W_{50}{}^{c}$, in km s^{-1} (see Catinella et al. 2012b). No inclination or turbulent motion corrections are applied.
Col. (8): observed, integrated HI-line flux density in Jy km s^{-1}, $F \equiv \int S\ dv$, measured on the smoothed and baseline-subtracted spectrum. The reported uncertainty is the sum in quadrature of the statistical and systematic errors (see Catinella et al. 2010 for details).
Col. (9): *rms* noise of the observation in mJy, measured on the signal- and RFI-free portion of the smoothed spectrum.
Col. (10): signal-to-noise ratio of the HI spectrum, S/N, estimated following ALFALFA and GASS (see *e.g.* Catinella et al. 2010).
Col. (11): base-10 logarithm of the HI mass, $M_{\rm HI}$, in solar units, computed via:

$$\frac{M_{\rm HI}}{\rm M_\odot} = \frac{2.356\times10^5}{1+z}\left[\frac{d_{\rm L}(z)}{\rm Mpc}\right]^2\left(\frac{\int S\ dv}{\rm Jy\ km\ s^{-1}}\right) \qquad (1)$$

where $d_{\rm L}(z)$ is the luminosity distance to the galaxy at redshift z as measured from the HI spectrum.
Col. (12): base-10 logarithm of the HI mass fraction, $M_{\rm HI}/M_\star$.
Col. (13): quality flag, Q. Code 1 indicates detections with a S/N ratio of 6.0 or higher. Code 2 is assigned to lower S/N, but still secure detections, and code 3 to marginal detections. The separation between codes 2 and 3 is not simply by S/N, but takes into account HI profile and baseline quality — code 3 detections have more uncertain HI parameters, hence are shown with different symbols in our plots. In all cases, the HI redshift is consistent with the SDSS measurement.
Col. (14): Arecibo project identifier (see Table 1).

For the 10 galaxies that were not detected (see section 2) we did not obtain stringent constraints on the HI masses — the upper limits are comparable to or higher than the HI masses of the detections. This is because, after the initial 1 or 2 hours of on-source integration, we completed the observations of the target only if there was a hint of galaxy HI emission at the expected frequency.

SDSS postage stamp images and HI spectra of the HIGHz detections can be found in the Appendix. Fig. 4 presents the distributions of measured redshifts, rotational velocities and HI masses for both high-quality (hatched) and marginal (solid histograms) detections. The HIGHz galaxies have HI masses that vary between 1.9 and 7.9 $\times10^{10}$ M$_\odot$, at the top end of the HI mass function (HIMF; Martin et al. 2010). Because the HIMF drops rapidly above $\log M_{\rm HI,*}/\rm M_\odot = 9.96$, these systems are rare in the local Universe (for instance, galaxies with $M_{\rm HI}\geq 5\times10^{10}$ M$_\odot$ are over a factor of 100 less common than $M_{\rm HI,*}$ ones).

4.2 SDSS and GALEX data

This section summarizes the quantities derived from optical and UV data used in this paper. All the optical parameters listed below were obtained from Structured Query Language (SQL) queries to the SDSS DR7 database server[1], unless otherwise noted.

The NUV magnitudes for our sample were obtained from the *GALEX Unique Source Catalogs*[2] (Seibert et al. 2012). The measured NUV$-r$ colors are corrected for Galactic extinction following Wyder et al. (2007), from which we obtained $A_{NUV}-A_r = 1.9807A_r$ (where the extinction A_r is available from the SDSS data base and reported in Table 3 below). We did not apply internal dust attenuation corrections.

Table 3 lists the relevant SDSS and UV quantities for the galaxies published in this work, ordered by increasing right ascension:
Cols. (1) and (2): AGC and SDSS identifiers.
Col. (3): SDSS redshift, $z_{\rm SDSS}$. The average uncertainty of SDSS redshifts for this sample is 0.00015.
Col. (4): base-10 logarithm of the stellar mass, $M_\star$, in solar units. Stellar masses are from the MPA/JHU SDSS DR7 catalog[3], and are derived from SDSS photometry using the methodology described in Salim et al. (2007, a Chabrier 2003 initial mass function is assumed). In one case, we replaced the SDSS stellar mass estimate with a different one (AGC 232041, see below).
Cols. (5) and (6): radii containing 50% and 90% of the Petrosian flux in r-band, R_{50} and R_{90} respectively, in arcsec.
Col. (7): radius containing 90% of the Petrosian flux in r-band, R_{90}, in kpc.
Col. (8): base-10 logarithm of the stellar mass surface density, $\mu_\star$, in M$_\odot$ kpc^{-2}. This quantity is defined as $\mu_\star = M_\star/(2\pi R_{50}^2)$, with R_{50} in kpc units.
Col. (9): Galactic extinction in r-band, ext$_r$, in magnitudes, from SDSS.
Col. (10): r-band model magnitude from SDSS, r, corrected for Galactic extinction.
Col. (11): minor-to-major axial ratio from the exponential fit in r-band, $(b/a)_r$, from SDSS.
Col. (12): inclination to the line-of-sight in degrees, computed from $(b/a)_r$ in the previous column assuming an intrinsic axial ratio $q_0 = 0.20$ as in Catinella et al. (2012a).
Col. (13): total star formation rate (SFR) in M$_\odot$ yr^{-1}, from the MPA/JHU SDSS DR7 catalog. These SFRs are based on the technique discussed in Brinchmann et al. (2004).
Col. (14): NUV$-r$ observed color, corrected for Galactic extinction.
Col. (15): source of the UV photometry: GALEX All-sky Imaging Survey (AIS) or Medium Imaging Survey (MIS; see Martin et al. 2005).

All our targets have SDSS MPA/JHU stellar masses in the interval $\log M_\star/\rm M_\odot = [10.3, 11.4]$ except for AGC 232041, which has an unreasonably large value of $\log M_\star/\rm M_\odot = 12.37$. Hence we computed new stellar mass estimates from the i-band luminosity and the $g-i$ colour following Zibetti, Charlot & Rix (2009), and applying k corrections based on analytical approximations by Chilingarian, Melchior & Zolotukhin (2010). For the other galaxies in our sample there is an excellent correlation between these estimates and the MPA/JHU values, with an offset of 0.21 dex (Zibetti's values are systematically larger). Hence we replaced the stellar mass of AGC 232041 with the new estimate, $\log M_\star/\rm M_\odot = 11.05$ (after subtracting the systematic offset), which falls well within the stellar mass interval of the other galaxies in our sample. This galaxy is identified by a different symbol in our plots.

[1] *http://cas.sdss.org/dr7/en/tools/search/sql.asp*
[2] *http://archive.stsci.edu/prepds/gcat/*
[3] *http://www.mpa-garching.mpg.de/SDSS/DR7/*; we used the improved stellar masses from *http://home.strw.leidenuniv.nl/~jarle/SDSS/*

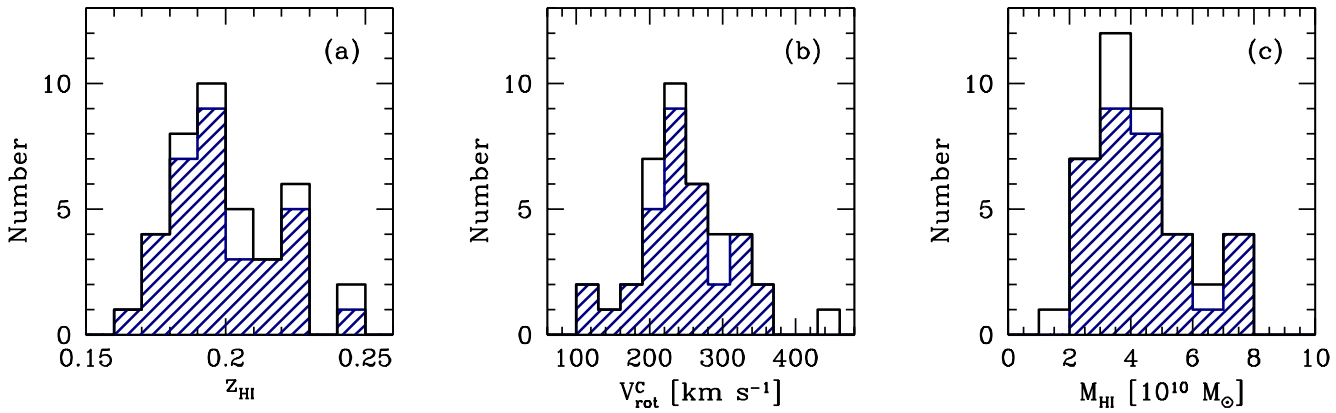

Figure 4. Distributions of (a) redshifts, (b) rotational velocities, and (c) HI masses for this sample (solid histograms). Hatched histograms do not include the marginal detections.

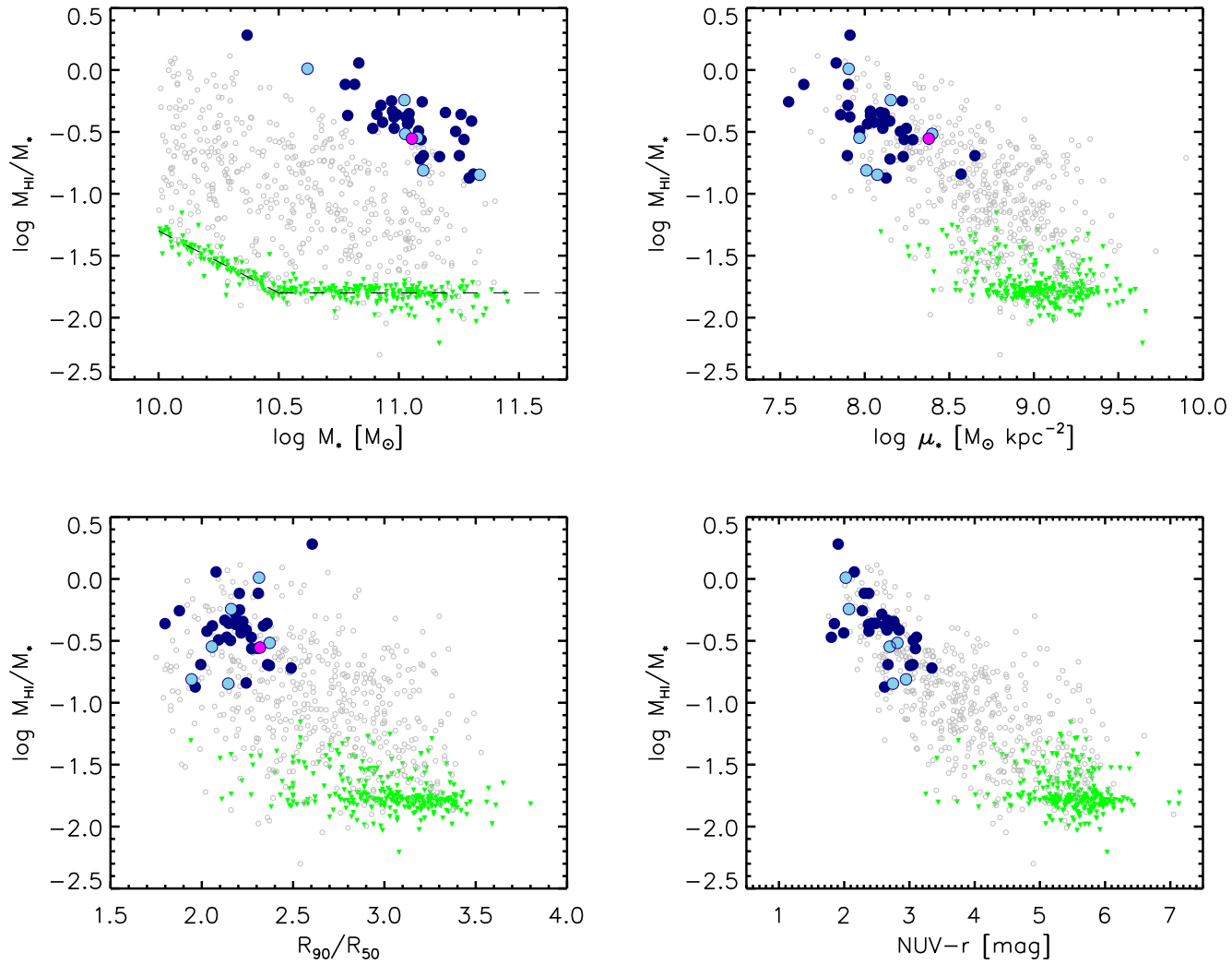

Figure 5. Gas fraction scaling relations. The HI mass fraction of the sample is plotted here as a function of stellar mass, stellar mass surface density, concentration index, and observed NUV−*r* colour (large blue symbols; light blue circles are marginal detections, and the magenta circle indicates AGC 232041 – see text). For comparison, we also show the HI detections (gray dots) and the non-detections plotted at their upper limits (green upside-down triangles) from the GASS sample. The dashed line in the top-left panel indicates the HI detection limit of GASS.

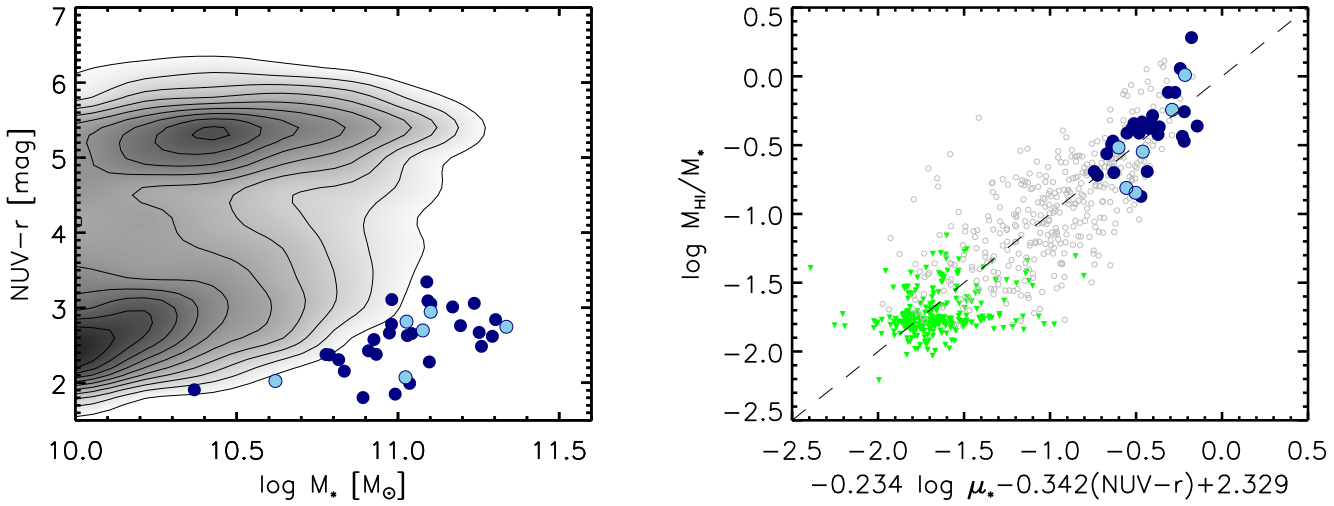

Figure 6. *Left:* NUV−r colour-stellar mass diagram. Contours and grayscales show the distribution of the GASS parent sample for comparison; blue symbols indicate HIGHz galaxies as in Fig. 5. Galaxies in the HIGHz sample are unusually blue for their stellar masses. *Right:* GASS gas fraction plane, showing the relation between measured (y axis) and predicted (x axis) HI mass fractions; the dashed line indicates the 1:1 relation, and the symbols are as in Fig. 5. The HIGHz galaxies are *not outliers* in this relation.

5 RESULTS

By selection, the HIGHz sample includes unusually HI-rich galaxies (see Fig. 4). Are these the tip of the iceberg of the $z \sim 0.2$ disk galaxy population, or just peculiar objects? Are their huge gas reservoirs due to recent accretion, or are these systems simply scaled-up versions of local gas-rich disks?

The properties of the HIGHz systems are best understood when compared with those of a representative sample of local galaxies with similar stellar masses, for which homogeneous HI measurements are available. Such a reference sample is uniquely provided by GASS, which measured the HI content of ~800 galaxies selected only by stellar mass ($10 < \log(M_\star/M_\odot) < 11.5$) and redshift ($0.025 < z < 0.05$). Not only GASS and HIGHz span the same stellar mass interval, but the HI observations were also taken and processed in the same way. We use here the final data release of GASS (Catinella et al. 2013) and, for comparisons that do not involve the gas content, the full *parent sample*, which is the super-set of 12,006 galaxies meeting GASS selection criteria out of which the targets for Arecibo observations were extracted.

We plot the HIGHz galaxies on the main gas fraction scaling relations identified by GASS in Fig. 5. Clockwise from the top left, we show how the gas mass fraction $M_{\rm HI}/M_\star$ depends on stellar mass, stellar mass surface density, observed NUV−r color (a proxy for specific star formation rate, or star formation rate per unit of stellar mass) and concentration index R_{90}/R_{50} (a proxy for bulge-to-total ratio) for both samples. HIGHz HI detections are shown as dark blue circles, while marginal detections are presented in light blue; the magenta circle is AGC 232041, for which we computed our own estimate of stellar mass (see § 4.2). GASS detections and non-detections are indicated by gray dots and green triangles, respectively. For consistency with HIGHz, we recomputed stellar mass surface densities for GASS using r-band Petrosian radii (as opposed to z-band, as in the GASS data release papers).

The gas fraction versus stellar mass plot confirms that the HIGHz sample is extremely HI-rich: these galaxies have $M_{\rm HI}/M_\star$ ratios that are a factor ~10 higher than the average value of GASS at the same stellar masses. These large gas fractions are comparable to those of Malin 1 (log $M_{\rm HI}/{\rm M}_\odot$= 10.82, log $M_\star/{\rm M}_\odot$= 10.88, Lelli, Fraternali & Sancisi 2010; Huang et al. 2014) and HIZOA J0836-43 (log $M_{\rm HI}/{\rm M}_\odot$= 10.88, log $M_\star/{\rm M}_\odot$= 10.64, Cluver et al. 2010), two of the most HI-massive galaxies known.

Interestingly, however, the large difference between HIGHz and GASS samples completely disappears if we consider the other scaling relations shown in Fig. 5. At fixed stellar mass surface density and NUV−r colour, HIGHz galaxies lie exactly on the trends followed by local massive galaxies. This automatically implies that, at fixed stellar mass, HIGHz galaxies should be outliers in the colour stellar mass diagram (and in the $\mu_\star$-$M_\star$ plot, see next section). Indeed, as shown in the left panel of Fig. 6, HIGHz galaxies lie outside the region that includes most of the GASS parent sample, indicated by the gray contours. Specifically, the $z \sim 0.2$ galaxies are unusually blue for their stellar masses, and similar systems are rare in the local Universe. As NUV−r is an excellent proxy for specific star formation rate, this implies that HIGHz galaxies formed the bulk of their stars at later times than the typical massive galaxy at $z = 0$ (see also the next section). We note that the peculiarity of our galaxies would not appear in an optical colour magnitude diagram, as all our targets lie on the optical red sequence. This is not surprising because, at such high stellar masses, optical colours do not properly trace current star formation activity (*e.g.*, Cortese 2012).

The results presented in Fig. 5 support the idea that the HI content of galaxies is mainly driven by their colour and stellar mass surface density, with the trend with stellar mass being just a secondary, not physically driven relation (*e.g.*, Catinella et al. 2010; Fabello et al. 2011). This is reinforced in the right panel of Fig. 6, which shows the gas fraction plane defined by GASS. This is a relation between the gas fraction measured by our HI observations and that predicted from the NUV−r colors and stellar surface densities of the galaxies. We use here the gas fraction prediction calibrated on GASS galaxies with NUV−$r \leq$ 4.5 mag (see Catinella et al. 2013)[4], which is clearly the most appropriate for

[4] The calibration of the gas fraction plane was obtained with z-band stellar

HIGHz. Our $z \sim 0.2$ galaxies follow the same relation identified by GASS, implying that their gas content is exactly what is expected based on their colours and stellar mass surface densities.

Lastly, also the rotational velocities of HIGHz galaxies are consistent with those expected from nearby systems. This is shown in Fig. 7, which reproduces the baryonic Tully-Fisher (TF) relation for the subset of GASS galaxies with inclinations larger than 40° and $R_{90}/R_{50} \leq 2.8$ from Catinella et al. (2012a). Our sample meets these two criteria by selection (see Fig. 5 and Table 3), except for two galaxies with inclinations slightly below the cut (37° and 39°) that we show anyway. Overall, the $z \sim 0.2$ sample lies on the baryonic TF relation, except for three outliers on the low velocity side (from top to bottom, these are AGC 181593, 191728 and 122040) and a marginal HI detection (AGC 249560) on the high velocity side. Notice however that there are similar outliers at lower baryonic mass also in GASS.

To summarize, the comparison with GASS shows that the HIGHz galaxies have unusually high gas content (in terms of both HI mass and HI gas fraction) and blue NUV$-r$ colors for their stellar mass, but are not outliers in the other scaling relations, including the gas fraction plane. Their low values of stellar mass surface density and concentration index are typical of disk-dominated systems, and star formation appears to proceed as expected, despite their huge HI reservoirs, with specific SFRs that are on average one order of magnitude larger than those of GASS HI detections. In other words, all observational evidence suggests that the HIGHz galaxies are rare, scaled-up versions of disk galaxies in the local Universe, with no clear signs of peculiarity or recent interaction. Hence, although these objects are not spatially resolved in HI, it seems reasonable to assume that their HI is distributed in a disk as well, rotating at the expected velocity given the baryonic mass of the system.

Incidentally, the results presented above should also dispel any doubts that our HI observations might be significantly contaminated by beam confusion. This is because, if we had detected the integrated HI emission of multiple galaxies within the beam instead, the HIGHz systems would be outliers in the gas fraction plane and/or the baryonic TF relation. This suggests that the effect of beam confusion, if present, is well within our observational uncertainties, as expected given our careful target selection (see Section 2).

6 DISCUSSION

Having established how HIGHz galaxies compare to the typical massive systems in the local Universe, we turn our attention to how these might fit into our general picture of galaxy evolution. On one side, we ask whether HI reservoirs as large as the ones we observed are still present at $z \sim 0$, despite being rare, or have completely disappeared. On the other side, it is natural to wonder if HIGHz galaxies might be the progeny of the very gas-rich turbulent disks observed at $z \sim 1$ (Tacconi et al. 2013). To answer these questions, we compare HIGHz to some of the most gas-rich samples (with stellar masses above 10^{10} $M_\odot$) currently known between $z \sim 0$ and ~ 1.

surface densities, hence the coefficients shown in Fig. 6 are strictly for z-band $\mu_\star$, but we plotted r-band $\mu_\star$ instead. Because the difference between z-band and r-band calibrations is barely noticeable, we prefer not to provide a new version of the gas fraction plane in this paper, and simply note that this small difference does not affect our conclusions at all.

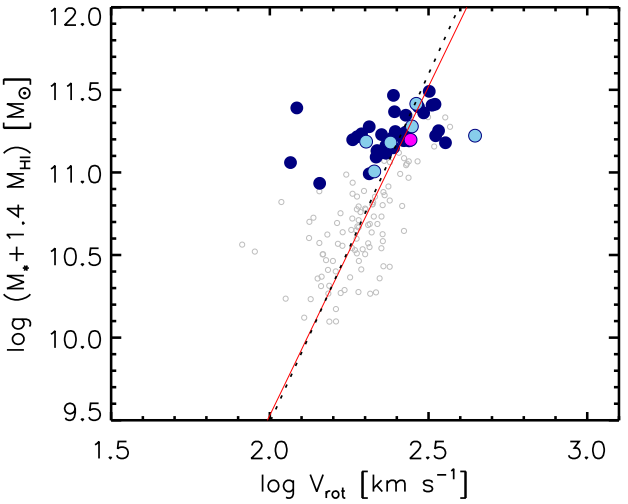

Figure 7. Baryonic Tully-Fisher relation. Gray dots are the "Tully-Fisher subset" of inclined, disk-dominated GASS galaxies, reproduced from Fig. 2 of Catinella et al. (2012a); the dotted line indicates the inverse fit to the GASS data points, which is in excellent agreement with the relation from McGaugh et al. (2000, red solid line). The HIGHz sample is shown with the same symbols used in Fig. 5.

6.1 Are there local analogs of the HIGHz galaxies?

As the most extreme example of massive, HI-rich galaxies at $z = 0$, we use the HIghMass (Huang et al. 2014) sample, a set of 34 exceptionally HI-rich local galaxies identified by ALFALFA. HIghMass galaxies were selected from the 40% ALFALFA data release (Haynes et al. 2011) to have both large HI mass (above 10^{10} $M_\odot$) and large HI gas fraction for their stellar mass (i.e. $M_{\rm HI}/M_\star$ more than 1 σ above the average, see their Fig. 1). Other samples of massive local galaxies claimed to be "unusually HI-rich" (*i.e.* Bluedisks, Wang et al. 2013, and the HI "Monsters", Lee et al. 2014) are, in fact, significantly less extreme than HIghMass in terms of gas fractions, and therefore are not shown in our plots. For consistency with our sample, we extracted stellar masses for HIghMass from the MPA/JHU SDSS DR7 catalog, and kept only galaxies with $\log(M_\star/M_\odot) \geq 10$. Stellar mass surface densities of HIghMass galaxies were computed using r-band petrosian radii and axis ratios obtained via elliptical aperture photometry of SDSS images (kindly provided by S. Huang, see Section 2 in Huang et al. 2014).

In Fig.8, we plot both HIGHz (blue) and HIghMass (red) on some of the main scaling relations followed by local galaxies. It is clear that HIghMass and HIGHz galaxies have similarly high HI gas fractions for their stellar masses (top-left panel), implying that $z = 0$ analogs of our galaxies do indeed exist. The fact that some of the $z \sim 0.2$ galaxies have more extreme gas fractions is not unexpected, as these were selected from a much larger volume (hence they are rarer) than the ALFALFA galaxies (which have $z < 0.06$). Moreover, both samples lie preferentially on the upper envelope of the main sequence of star-forming galaxies (dashed line in the bottom-right panel, from eq. 12 of Salim et al. 2007, which applies to galaxies with NUV$-r<$ 4 mag), confirming that their large HI reservoir is actively feeding the formation of new stars at a significant rate, as already hinted by Fig. 6.

Intriguingly, the only clear difference between HIGHz and HIghMass is in their stellar distribution (bottom-left panel): HIGHz systems have stellar surface densities that are ∼0.6 dex smaller than

HIghMass, implying that their optical radii are significantly larger than what observed in local, massive disks[5]. This is purely a selection effect since, as mentioned in Sec. 2, we intentionally picked the galaxies *with the largest apparent sizes from the SDSS images* as targets for Arecibo observations. Therefore, we ended up with a sample of very uncommon galaxies, even rarer than HIghMass.

As discussed by Huang et al. 2014, the low $\mu_\star$ values of HIghMass compared to the rest of ALFALFA points out to their large halo spin parameters. It is a well-known prediction of galaxy formation models that stellar disks formed in dark matter halos with higher angular momentum content are more extended and have higher gas fractions (*e.g.*, Mo, Mao & White 1998; Boissier & Prantzos 2000). Hence, HIGHz galaxies are most likely the tail of the high spin parameter distribution identified by HIghMass. Indeed, the gas fractions of HIGHz galaxies are consistent with the values predicted for spin parameters in the range ∼0.07-0.09 (Boissier & Prantzos 2000). This confirms that the HI content, SFR and stellar distribution of our galaxies are what expected from their mass and angular momentum, and that no recent accretion and/or interaction (sometimes invoked to explain unusually gas-rich galaxies, *e.g.* Cluver et al. 2010) are required.

Lastly, HIGHz (and HIghMass, as discussed in Huang et al. 2014) systems are not analogs of giant low surface brightness galaxies like Malin 1 (Bothun et al. 1987). Indeed, the low SFR of Malin 1 (∼0.1 $M_\odot$ yr^{-1}, Impey & Bothun 1989, but see also Lelli, Fraternali & Sancisi 2010) indicates that its huge HI reservoir (log $M_{\rm HI}/M_\odot$=10.83, Pickering et al. 1997; Lelli, Fraternali & Sancisi 2010) is largely inert, whereas HIGHz galaxies are actively star-forming, with an average SFR of 13.5 $M_\odot$ yr^{-1} (see Table 1). This is demonstrated by the fact that the average depletion time ($M_{\rm HI}$/SFR) of HIGHz systems is ∼3 Gyr, in line with the typical value observed in normal star-forming galaxies (Schiminovich et al. 2010; Boselli et al. 2014).

6.2 How do HIGHz galaxies compare with turbulent gas-rich disks at z ∼1?

As a representative sample of the high gas fraction population of z ∼1 disks we consider PHIBSS, the IRAM Plateau de Bure HIghz Blue Sequence CO(3-2) Survey (Tacconi et al. 2013). PHIBSS measured the molecular gas content of 52 star-forming galaxies in two redshift slices, at $z \sim 1.2$ and 2.2; most of these systems are rotationally supported turbulent disks. Here we restrict the PHIBSS sample to the 38 galaxies in the lower redshift interval ($1.00 < z < 1.53$), which all have CO detections.

We also include in this comparison DYNAMO (DYnamics of Newly-Assembled Massive Objects, Green et al. 2014), a survey of local star-forming galaxies selected by Hα emission from the SDSS to be potential analogs of the PHIBSS systems. Although for DYNAMO there are no direct HI observations, and molecular gas measurements are available for only four objects (Fisher et al. 2014), given their possible connection to high-redshift galaxies it is very interesting to see how they relate to our HIGHz sample. As for HIghMass, we extract stellar masses and stellar surface densities for DYNAMO from SDSS, consistently with our sample.

[5] We checked the reliability of our $\mu_\star$ measurements by taking into account the effect of seeing on the stellar radii (the median seeing at r-band is 1.43″, according to the SDSS DR7 web site), and the conclusion remains the same, as most points in the plot would move upward by less than the symbol size.

In order to compare the gas content of all samples, which have HI (HIGHz, HIghMass) or H_2 (PHIBSS) measurements, or total gas masses simply inferred from SFRs (DYNAMO), we estimate total gas masses as follows. For GASS, HIGHz, and HIghMass we assume a molecular-to-atomic hydrogen mass ratio $M_{H_2}/M_{\rm HI}$=0.3, which is the average value measured for a representative subset of GASS galaxies by COLD GASS (Saintonge et al. 2011). Hence, M_{gas} = 1.768 $M_{\rm HI}$ for these samples, taking into account the Helium contribution (a factor 1.36). It should be kept in mind that these are rough estimates, as the relation between M_{H_2} and $M_{\rm HI}$ in this stellar mass regime has a large scatter (0.41 dex, see Fig. 8 in Saintonge et al. 2011). For DYNAMO, we use their published total gas content estimates, which were inferred from the star formation rate densities using the Kennicutt-Schmidt (KS; Kennicutt 1998) law, and correct them for the Helium contribution as above. We assume the same $M_{H_2}/M_{\rm HI}$ ratio obtained from GASS to compute M_{gas} for the four galaxies with available CO data. For PHIBSS, we assume that the hydrogen is all in molecular phase, *i.e.* $M_{gas} = M_{H_2}$ (Tacconi et al. 2013; their measurements already include the He contribution).

The results of our comparisons are again presented in Fig. 8. Keeping in mind all the assumptions in our calculations, the top-right panel shows that the total gas content of the bulk of $z \sim 1.2$ galaxies is comparable to that of both HIGHz and HIghMass, although the partition between atomic and molecular phases is obviously very different. It is beyond the reach of current and upcoming radio facilities to detect HI emission from individual PHIBSS galaxies, but only the presence of large HI reservoirs that are unaccounted for (and considered unlikely by current simulations, *e.g.* Lagos et al. 2014; Popping, Somerville & Trager 2014) can make the bulk of PHIBSS galaxies significantly different from HIGHz and HIghMass.

Conversely, DYNAMO galaxies have less overlap with the other three samples considered here. Indeed, DYNAMO does not include galaxies with stellar masses above ∼ 10^{11} $M_\odot$, hence the parameter space in common with HIGHz and PHIBSS is somewhat limited. Because DYNAMO gas fractions are only estimates, we also plot the four galaxies with actual CO measurements (dark green squares, connected by lines to the corresponding KS estimates), which agree pretty well with the KS predictions. Thus, taking all the predicted gas masses at face value, about half of DYNAMO systems seem to have gas fractions as extreme as those of the other samples.

Despite their similar total gas fractions, PHIBSS and HIGHz samples are remarkably different when we look at their SFRs and stellar mass surface densities in the bottom panels of Fig. 8. Firstly, as expected, the SFRs (and hence star formation efficiency) of PHIBSS galaxies are significantly higher (∼1 dex) than all the other samples considered here. Secondly, the average stellar mass surface densities of PHIBSS systems (as well as those of HIghMass and DYNAMO) are entirely consistent with those of disk-dominated, local galaxies with similar stellar masses, and only a couple of objects exhibit values of $\mu_\star$ comparable to those of HIGHz. As mentioned in the previous section, the fact that HIGHz galaxies occupy a region of parameter space in the $\mu_\star$- $M_\star$ diagram that is practically untouched by the other samples is the result of a selection effect. As we are looking at two families of galaxies separated by ∼6 Gyr of evolution, the differences in optical and SFR properties between HIGHz and PHIBSS samples are not surprising, and it is interesting to speculate whether or not we can confidently exclude an evolutionary link between the two.

If PHIBSS galaxies are representative of the massive popu-

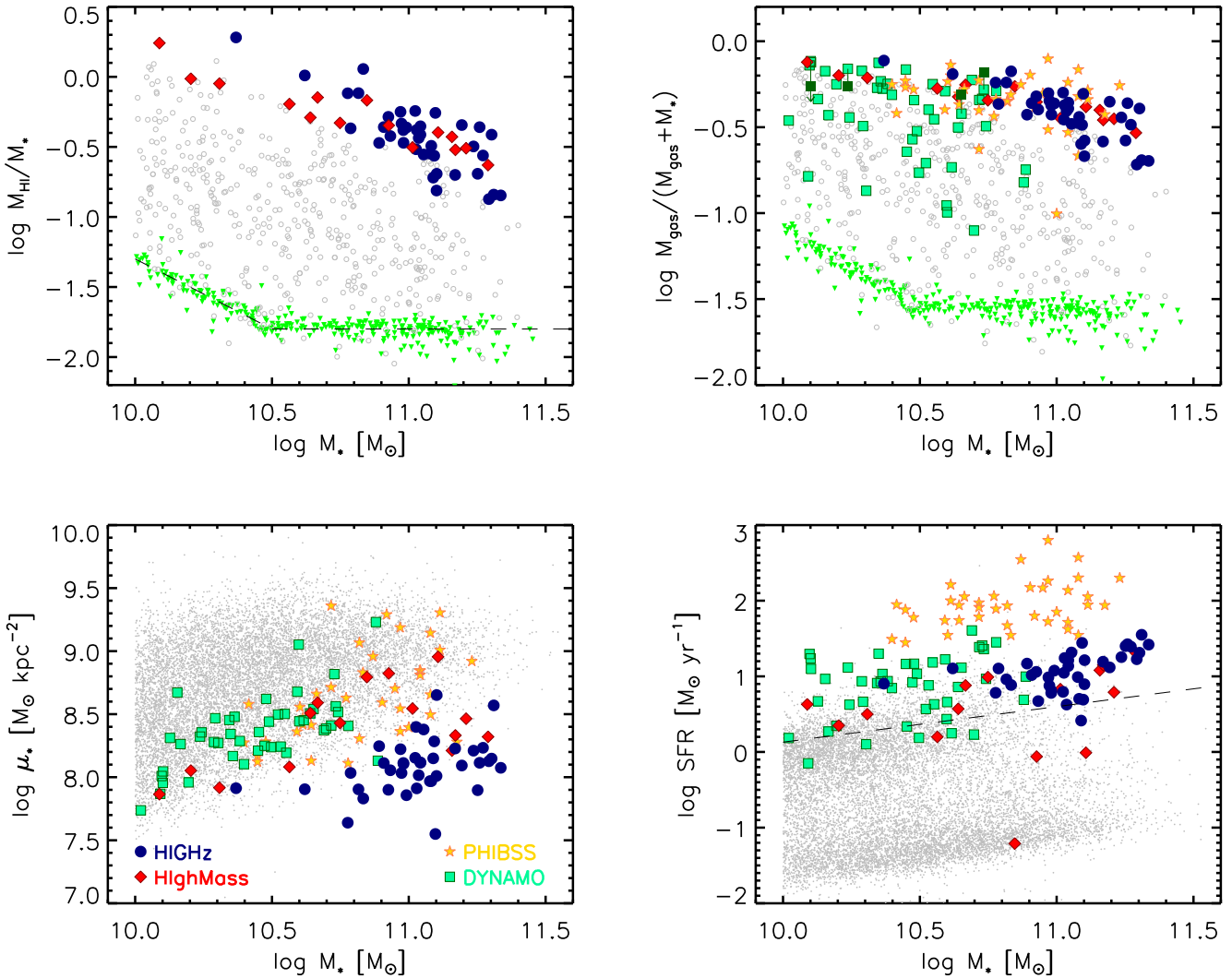

Figure 8. Comparison with literature samples. *Top left:* HI gas fraction versus stellar mass, as in Fig. 5; HIGHz and HIghMass galaxies with stellar masses larger than 10^{10} $M_\odot$ are shown as blue circles and red diamonds, respectively. *Top right:* Total gas fraction versus stellar mass (see text for details on how the total gas fractions are computed). Stars and green squares indicate PHIBSS and DYNAMO galaxies, respectively; dark green squares connected by lines are the four DYNAMO systems with available CO measurements (the leftmost one is an upper limit, as shown by the downward arrow). *Bottom left:* The stellar surface density is plotted as a function of stellar mass for the same data sets; gray dots show the full GASS parent sample. *Bottom right:* Star formation rate as a function of stellar mass, same symbols as bottom left panel. A dashed line indicates the star-forming main sequence from Salim et al. (2007, eq. 12).

lation at z ~1, it would be extremely hard to explain why typical massive galaxies at z ~1 evolve into such a rare population of gas-rich systems as HIGHz. Conversely, if gas-rich z ~1 systems are the tip of the iceberg of the high-redshift population of disk galaxies, as hinted by recent numerical simulations (*e.g.* Lagos et al. 2014; Popping, Somerville & Trager 2014), the main obstacle to reconcile the two populations is just the difference in $\mu_\star$, which would require significant disk growth from z ~1.2 to ~0.2. Observations and semi-analytical models (Dutton et al. 2011) suggest that, between z ~1 and 0, a massive disk galaxy increases its stellar mass by a factor of ~2.5 and its radius by a factor of ~2. This implies a decrease in $\mu_\star$ of ~0.2 dex. Although this shift is too small to reconcile HIGHz and PHIBSS galaxies, it is intriguing to note that, once HIGHz and HIghMass are treated as a single population of "local" HI massive systems, the differences with the population of gas-rich turbulent disks at high-redshift almost entirely disappear.

Unfortunately, until a proper characterization of the gas properties of a representative population of disk galaxies at z ~1 is obtained, it is impossible to establish whether gas-rich galaxies at various redshifts are really linked, and this discussion remains just an intriguing speculation. Nevertheless, our findings highlight the importance of investigating the still vastly unexplored regime of very high gas content for our understanding of galaxy evolution across cosmic time.

7 SUMMARY AND CONCLUSIONS

In this paper we presented HIGHz, a survey that measured the HI content of 39 disk galaxies at redshift z ~ 0.2 using the Arecibo radio telescope. This sample includes the highest-redshift detections of HI emission from individual galaxies published to date, which are also among the most HI-massive systems known. By selection, HIGHz galaxies are disk-dominated systems in relatively

isolated fields, with stellar masses $M_\star$= 2-22 $\times 10^{10}$ M$_\odot$, HI masses $M_{\rm HI}$= 2-8 $\times 10^{10}$ M$_\odot$, star formation rates of 3-35 M$_\odot$ yr^{-1} and redshifts z = 0.17-0.25.

We showed that the HIGHz galaxies have unusually large HI gas fractions and blue NUV$-r$ colours for their stellar masses. However, when we look at more physical relations, such as the gas fraction plane and the baryonic Tully-Fisher relation, HIGHz galaxies are indistinguishable from the average systems. In other words, their gas content is exactly what is expected from their UV and optical properties, and there is nothing unusual in the way in which star formation proceeds in these galaxies, or in the relation between their dynamical and baryonic masses. We concluded that HIGHz galaxies are rare, scaled-up versions of disk galaxies in the local Universe, and there is no need to invoke unusual episodes of gas accretion to explain their large reservoirs.

When compared to HIghMass, which includes the most HI-rich local galaxies extracted from the HI-blind ALFALFA survey, HIGHz systems show striking similarities in their gas content and star formation. The only significant difference is that, by selection, HIGHz galaxies have ∼0.6 dex lower stellar surface densities, suggesting higher values of their spin parameters. Therefore HIghMass galaxies appear to be the local counterparts of HIGHz, with the latter mapping into the high end of the spin parameter distribution of HIghMass.

It is more difficult to establish a connection with the gas-rich, turbulent disks identified by PHIBSS at $z \sim 1$. It is intriguing that the total gas content of HIGHz and PHIBSS seems to be similar (although the phase is clearly different) but, unless the PHIBSS disks are not representative of the general disk population at $z \sim 1$, it is very unlikely that they could be the progenitors of such a rare population at $z \sim 0.2$.

In addition to probing the HI Universe beyond $z = 0.2$ for the first time with direct detections, the HIGHz survey provides important insights into the properties of the massive, HI-rich systems that will likely dominate the samples detected at higher redshift by future HI surveys with the SKA and its precursor telescopes. This is particularly relevant for deep HI surveys such as DINGO (Deep Investigation of Neutral Gas Origins, Meyer 2009) and especially LADUMA (Looking At the Distant Universe with the MeerKAT Array, Holwerda, Blyth & Baker 2012), which will open the higher redshift Universe to HI exploration.

ACKNOWLEDGMENTS

We wish to thank Shan Huang for kindly providing us with HIghMass data in advance of publication. BC warmly thanks Martha P. Haynes and Riccardo Giovanelli for their contributions to the initial stages of the survey, and Phil Perillat, Ganesh Rajagopalan and the telescope operators at Arecibo for their help and assistance. We thank our referee, Bärbel Koribalski, for useful comments that helped us improving the clarity of our manuscript. BC is the recipient of an Australian Research Council Future Fellowship (FT120100660). LC acknowledges support under the Australian Research Council's Discovery Projects funding scheme (DP130100664).

This research has made use of the NASA/IPAC Extragalactic Database (NED) which is operated by the Jet Propulsion Laboratory, California Institute of Technology, under contract with the National Aeronautics and Space Administration.

The Arecibo Observatory is operated by SRI International under a cooperative agreement with the National Science Foundation (AST-1100968), and in alliance with Ana G. Méndez-Universidad Metropolitana, and the Universities Space Research Association.

GALEX (Galaxy Evolution Explorer) is a NASA Small Explorer, launched in April 2003. We gratefully acknowledge NASA's support for construction, operation, and science analysis for the GALEX mission, developed in cooperation with the Centre National d'Etudes Spatiales (CNES) of France and the Korean Ministry of Science and Technology.

Funding for the SDSS and SDSS-II has been provided by the Alfred P. Sloan Foundation, the Participating Institutions, the National Science Foundation, the U.S. Department of Energy, the National Aeronautics and Space Administration, the Japanese Monbukagakusho, the Max Planck Society, and the Higher Education Funding Council for England. The SDSS Web Site is http://www.sdss.org/.

The SDSS is managed by the Astrophysical Research Consortium for the Participating Institutions. The Participating Institutions are the American Museum of Natural History, Astrophysical Institute Potsdam, University of Basel, University of Cambridge, Case Western Reserve University, University of Chicago, Drexel University, Fermilab, the Institute for Advanced Study, the Japan Participation Group, Johns Hopkins University, the Joint Institute for Nuclear Astrophysics, the Kavli Institute for Particle Astrophysics and Cosmology, the Korean Scientist Group, the Chinese Academy of Sciences (LAMOST), Los Alamos National Laboratory, the Max-Planck-Institute for Astronomy (MPIA), the Max-Planck-Institute for Astrophysics (MPA), New Mexico State University, Ohio State University, University of Pittsburgh, University of Portsmouth, Princeton University, the United States Naval Observatory, and the University of Washington.

REFERENCES

Abazajian K. et al., 2004, AJ, 128, 502
Abazajian K. et al., 2005, AJ, 129, 1755
Abazajian K. et al., 2003, AJ, 126, 2081
Abazajian K. N. et al., 2009, ApJS, 182, 543
Adelman-McCarthy J. K. et al., 2007, ApJS, 172, 634
Barnes D. G. et al., 2001, MNRAS, 322, 486
Bell E. F. et al., 2005, ApJ, 625, 23
Boissier S., Prantzos N., 2000, MNRAS, 312, 398
Booth R. S., de Blok W. J. G., Jonas J. L., Fanaroff B., 2009, ArXiv e-prints
Boselli A., Cortese L., Boquien M., Boissier S., Catinella B., Lagos C., Saintonge A., 2014, A&A, 564, A66
Bothun G. D., Impey C. D., Malin D. F., Mould J. R., 1987, AJ, 94, 23
Brinchmann J., Charlot S., White S. D. M., Tremonti C., Kauffmann G., Heckman T., Brinkmann J., 2004, MNRAS, 351, 1151
Carilli C. L., Rawlings S., 2004, New Astronomy Reviews, 48, 979
Catinella B., Haynes M. P., Giovanelli R., 2007, AJ, 134, 334
Catinella B., Haynes M. P., Giovanelli R., Gardner J. P., Connolly A. J., 2008, ApJL, 685, L13
Catinella B. et al., 2012a, MNRAS, 420, 1959
Catinella B. et al., 2013, MNRAS, 436, 34
Catinella B. et al., 2012b, A&A, 544, A65
Catinella B. et al., 2010, MNRAS, 403, 683
Chabrier G., 2003, PASP, 115, 763
Chilingarian I. V., Melchior A.-L., Zolotukhin I. Y., 2010, MNRAS, 405, 1409

Cluver M. E., Jarrett T. H., Kraan-Korteweg R. C., Koribalski B. S., Appleton P. N., Melbourne J., Emonts B., Woudt P. A., 2010, ApJ, 725, 1550
Cortese L., 2012, A&A, 543, A132
Cortese L., Catinella B., Boissier S., Boselli A., Heinis S., 2011, MNRAS, 415, 1797
Daddi E. et al., 2010, ApJ, 713, 686
Dutton A. A. et al., 2011, MNRAS, 410, 1660
Fabello S., Catinella B., Giovanelli R., Kauffmann G., Haynes M. P., Heckman T. M., Schiminovich D., 2011, MNRAS, 411, 993
Fernández X. et al., 2013, ApJL, 770, L29
Fisher D. B. et al., 2014, ApJL, 790, L30
Fridman P. A., Baan W. A., 2001, A&A, 378, 327
Genzel R. et al., 2011, ApJ, 733, 101
Giovanelli R. et al., 2005, AJ, 130, 2598
Green A. W. et al., 2014, MNRAS, 437, 1070
Haynes M. P. et al., 2011, AJ, 142, 170
Holwerda B. W., Blyth S.-L., Baker A. J., 2012, in IAU Symposium, Vol. 284, IAU Symposium, Tuffs R. J., Popescu C. C., eds., pp. 496–499
Huang S., Haynes M. P., Giovanelli R., Brinchmann J., 2012, ApJ, 756, 113
Huang S. et al., 2014, ApJ, 793, 40
Impey C., Bothun G., 1989, ApJ, 341, 89
Jaffé Y. L., Poggianti B. M., Verheijen M. A. W., Deshev B. Z., van Gorkom J. H., 2012, ApJL, 756, L28
Johnston S. et al., 2008, Experimental Astronomy, 22, 151
Kennicutt, Jr. R. C., 1998, ApJ, 498, 541
Lagos C. D. P., Baugh C. M., Lacey C. G., Benson A. J., Kim H.-S., Power C., 2011, MNRAS, 418, 1649
Lagos C. D. P., Baugh C. M., Zwaan M. A., Lacey C. G., Gonzalez-Perez V., Power C., Swinbank A. M., van Kampen E., 2014, MNRAS, 440, 920
Lah P. et al., 2009, MNRAS, 399, 1447
Lee C., Chung A., Yun M. S., Cybulski R., Narayanan G., Erickson N., 2014, MNRAS, 441, 1363
Lelli F., Fraternali F., Sancisi R., 2010, A&A, 516, A11
Lilly S. J., Le Fevre O., Hammer F., Crampton D., 1996, ApJL, 460, L1+
Madau P., Ferguson H. C., Dickinson M. E., Giavalisco M., Steidel C. C., Fruchter A., 1996, MNRAS, 283, 1388
Martin A. M., Papastergis E., Giovanelli R., Haynes M. P., Springob C. M., Stierwalt S., 2010, ApJ, 723, 1359
Martin D. C. et al., 2005, ApJL, 619, L1
McGaugh S. S., Schombert J. M., Bothun G. D., de Blok W. J. G., 2000, ApJL, 533, L99
Meyer M., 2009, in Panoramic Radio Astronomy: Wide-field 1-2 GHz Research on Galaxy Evolution
Mo H. J., Mao S., White S. D. M., 1998, MNRAS, 295, 319
Obreschkow D., Rawlings S., 2009, ApJL, 696, L129
Papastergis E., Giovanelli R., Haynes M. P., Rodríguez-Puebla A., Jones M. G., 2013, ApJ, 776, 43
Pickering T. E., Impey C. D., van Gorkom J. H., Bothun G. D., 1997, AJ, 114, 1858
Popping G., Somerville R. S., Trager S. C., 2014, MNRAS, 442, 2398
Saintonge A. et al., 2011, MNRAS, 415, 32
Salim S. et al., 2007, ApJS, 173, 267
Schiminovich D. et al., 2010, MNRAS, 408, 919
Seibert M. et al., 2012, in American Astronomical Society Meeting Abstracts, Vol. 219, American Astronomical Society Meeting Abstracts #219, p. 340.01
Springob C. M., Haynes M. P., Giovanelli R., Kent B. R., 2005, ApJS, 160, 149
Tacconi L. J. et al., 2013, ApJ, 768, 74
van Zee L., Maddalena R. J., Haynes M. P., Hogg D. E., Roberts M. S., 1997, AJ, 113, 1638
Verheijen M., van Gorkom J. H., Szomoru A., Dwarakanath K. S., Poggianti B. M., Schiminovich D., 2007, ApJL, 668, L9
Wang J. et al., 2013, MNRAS, 433, 270
Wyder T. K. et al., 2007, ApJS, 173, 293
York D. G. et al., 2000, AJ, 120, 1579
Zibetti S., Charlot S., Rix H.-W., 2009, MNRAS, 400, 1181

Table 2. HI Properties of HI Detections.

AGC (1)	SDSS ID (2)	T_{on} (min) (3)	Δv (km s^{-1}) (4)	z (5)	W_{50} (km s^{-1}) (6)	$W_{50}{}^{c}$ (km s^{-1}) (7)	F (Jy km s^{-1}) (8)	rms (mJy) (9)	S/N (10)	Log M_{HI} ($M_\odot$) (11)	Log $M_{HI}/M_\star$ (12)	Q (13)	Project ID (14)
101750	J003610.70+142246.4	156	28	0.190872	543± 21	444	0.19± 0.03	0.12	8.2	10.51	−0.47	1	a1803f
101710	J003840.25+153912.9	88	27	0.176535	598± 4	497	0.16± 0.05	0.16	4.5	10.37	−0.72	2	1803f
122040	J020849.45+130442.5	56	27	0.168210	332± 23	273	0.34± 0.04	0.17	15.0	10.65	0.28	1	a1803f
181518	J082522.13+325953.6	112	27	0.171022	515± 23	428	0.26± 0.05	0.17	8.0	10.55	−0.36	1	a1803
181593	J084800.91+061837.2	176	29	0.220272	256± 9	198	0.13± 0.04	0.18	6.0	10.47	−0.84	1	a2008,a2270
181559	J085733.51+034456.8	132	28	0.189094	546± 13	447	0.25± 0.05	0.17	7.4	10.63	−0.41	1	a1803
198310	J090315.37+073332.4	230	29	0.217517	481± 3	383	0.15± 0.03	0.12	7.2	10.53	−0.56	1	a2270
191826	J091954.42+085344.0	116	28	0.189905	770± 21	636	0.42± 0.06	0.17	8.7	10.85	−0.34	1	a2008
191728	J091957.00+013851.6	96	27	0.176425	219± 6	174	0.18± 0.03	0.18	9.3	10.42	−0.47	1	a1803
191787	J094921.53+044239.7	104	28	0.190145	601± 5	493	0.26± 0.06	0.18	6.2	10.64	−0.33	1	a1803
191838	J095923.26+065109.1	72	38	0.189998	538± 13	436	0.19± 0.06	0.16	5.0	10.51	−0.52	3	a2008
202125	J102848.86+042331.9	112	28	0.207010	480± 17	386	0.10± 0.04	0.16	3.4	10.29	−0.81	3	a1803
208750	J105138.96+061751.7	90	41	0.223601	466± 79	364	0.15± 0.06	0.17	4.3	10.56	−0.69	2	a2428
208751	J105230.22+082324.3	110	28	0.187710	492± 23	403	0.19± 0.04	0.14	7.6	10.51	−0.42	1	a2428
212966	J110730.34+072350.2	124	36	0.206446	494± 16	395	0.13± 0.04	0.14	4.4	10.41	−0.69	2	a2008
212967	J111353.47+094959.7	150	34	0.247755	414± 5	318	0.15± 0.04	0.16	5.4	10.63	0.01	3	a2270
212941	J111645.15+054210.0	180	29	0.223625	383± 39	301	0.18± 0.04	0.17	7.0	10.63	−0.36	1	a1803
212887	J114634.33+053442.0	176	28	0.195732	772± 23	634	0.29± 0.04	0.11	9.0	10.72	−0.25	1	a1803
212871	J120052.83+033754.9	100	28	0.190208	742± 7	612	0.30± 0.06	0.17	6.2	10.71	−0.56	1	a1803
224321	J120948.14+100822.5	80	28	0.187520	417± 14	339	0.26± 0.05	0.19	8.9	10.64	−0.29	1	a2008
228389	J122036.32+081904.2	75	29	0.221760	377± 10	297	0.17± 0.05	0.18	6.3	10.60	−0.44	1	a2428
239110	J130434.51+271334.9	75	29	0.220002	533± 3	425	0.30± 0.05	0.18	8.3	10.84	−0.26	1	a2428
232041	J132325.27+043707.6	203	27	0.186225	591± 29	487	0.19± 0.04	0.12	7.5	10.50	−0.55	1	a1803,a2270
232046	J133327.34+042244.8	144	31	0.188360	818± 5	675	0.24± 0.05	0.14	5.1	10.60	−0.38	2	a1803,a2008
232055	J134211.36+053211.5	92	28	0.202987	464± 10	374	0.26± 0.05	0.18	8.4	10.70	−0.12	1	a2008
232127	J135949.19+052731.8	140	37	0.228068	604± 17	477	0.22± 0.05	0.14	6.1	10.74	−0.50	1	a2270
242091	J140522.72+052814.6	156	28	0.195302	502± 4	408	0.25± 0.04	0.13	10.3	10.65	−0.38	1	a1803
242073	J140856.04+051616.3	140	28	0.190625	422± 2	343	0.15± 0.03	0.13	7.4	10.42	−0.37	1	a2270
249558	J142151.16+100623.6	85	28	0.193841	383± 6	309	0.15± 0.03	0.14	7.2	10.42	−0.87	1	a2428
242147	J142735.69+033434.2	176	30	0.245370	499± 11	389	0.28± 0.05	0.18	8.0	10.90	−0.36	1	a1803
249559	J144518.88+025012.3	95	28	0.190355	331± 73	266	0.18± 0.04	0.18	7.3	10.47	−0.70	1	a2428
249560	J144823.96+125551.9	164	35	0.195415	771± 9	630	0.19± 0.04	0.12	5.0	10.53	−0.55	3	a2428
252580	J151337.28+041921.1	84	27	0.174961	478± 8	396	0.32± 0.06	0.21	8.4	10.66	−0.12	1	a1803
252654	J153240.56+323428.8	92	32	0.201136	792± 4	646	0.26± 0.06	0.16	5.0	10.69	−0.35	2	a2008
252641	J153400.67+001133.2	116	28	0.203574	591± 86	479	0.31± 0.09	0.29	4.8	10.78	−0.24	3	a1803
262026	J160433.51+310900.0	112	41	0.223168	642± 2	509	0.13± 0.05	0.14	3.2	10.49	−0.85	3	a2008,a2270
262029	J160938.00+312958.5	136	29	0.218648	642± 56	515	0.34± 0.05	0.15	9.0	10.89	−0.41	1	a2008
262033	J162515.41+280530.3	260	28	0.187113	643± 43	530	0.24± 0.03	0.11	9.4	10.59	−0.49	1	a2270
262015	J165940.12+344307.8	96	28	0.198331	504± 16	409	0.42± 0.05	0.19	12.0	10.89	0.06	1	a1803

Table 3. SDSS and UV Parameters.

AGC (1)	SDSS ID (2)	z_{SDSS} (3)	Log $M_\star$ ($M_\odot$) (4)	R_{50} ($''$) (5)	R_{90} ($''$) (6)	R_{90} (kpc) (7)	Log $\mu_\star$ ($M_\odot$ kpc^{-2}) (8)	ext$_r$ (mag) (9)	r (mag) (10)	(b/a)$_r$ (11)	incl (deg) (12)	SFR ($M_\odot$ yr^{-1}) (13)	NUV$-r$ (mag) (14)	GALEX (15)
101750	J003610.70+142246.4	0.1909	10.98	2.42	5.17	23.3	8.11	0.18	17.52	0.463	65	6.4	3.11	MIS
101710	J003840.25+153912.9	0.1769	11.09	2.84	7.07	29.3	8.15	0.16	17.59	0.390	70	2.6	3.34	MIS
122040	J020849.45+130442.5	0.1682	10.37	1.72	4.48	17.6	7.91	0.25	17.63	0.363	72	8.0	1.91	MIS
181518	J082522.13+325953.6	0.1709	10.91	2.50	5.37	21.4	8.11	0.12	17.49	0.429	67	10.4	2.43	MIS
181593	J084800.91+061837.2	0.2201	11.31	1.77	3.97	21.0	8.57	0.14	17.51	0.603	55	35.4	...	...
181559	J085733.51+034456.8	0.1894	11.04	2.59	5.74	25.7	8.12	0.13	17.50	0.516	61	13.7	2.66	MIS
198310	J090315.37+073332.4	0.2174	11.09	1.94	4.41	23.0	8.28	0.15	18.32	0.263	80	27.7	3.09	MIS
191826	J091954.42+085344.0	0.1899	11.19	3.16	7.03	31.5	8.09	0.14	17.43	0.280	79	13.1	2.76	AIS
191728	J091957.00+013851.6	0.1763	10.89	2.03	4.61	19.0	8.25	0.08	17.24	0.679	49	14.7	1.80	MIS
191787	J094921.53+044239.7	0.1903	10.97	2.62	5.57	25.0	8.03	0.11	17.66	0.475	64	7.5	2.66	MIS
191838	J095923.26+065109.1	0.1902	11.03	1.83	4.34	19.5	8.40	0.11	17.69	0.455	65	11.1	2.81	AIS
202125	J102848.86+042331.9	0.2069	11.10	2.84	5.52	27.2	8.01	0.09	17.74	0.341	74	7.9	2.95	MIS
208750	J105138.96+061751.7	0.2239	11.25	3.52	7.02	37.9	7.90	0.09	17.31	0.811	37	25.1	2.67	MIS
208751	J105230.22+082324.3	0.1880	10.93	2.47	5.01	22.2	8.06	0.07	17.57	0.461	65	4.7	2.38	MIS
212966	J110730.34+072350.2	0.2066	11.10	1.36	3.21	15.8	8.65	0.09	17.78	0.607	54	16.4	3.05	AIS
212967	J111353.47+094959.7	0.2482	10.62	1.50	3.47	21.0	7.90	0.06	18.40	0.683	48	12.7	2.02	AIS
212941	J111645.15+054210.0	0.2239	10.99	2.73	4.91	26.5	7.86	0.21	17.53	0.589	56	11.9	1.85	AIS
212887	J114634.33+053442.0	0.1961	10.97	2.03	4.48	20.8	8.22	0.05	17.78	0.360	72	9.7	...	...
212871	J120052.83+033754.9	0.1904	11.27	2.93	6.75	30.4	8.23	0.07	17.23	0.427	67	24.7	...	...
224321	J120948.14+100822.5	0.1879	10.93	2.93	6.40	28.4	7.90	0.07	17.27	0.698	47	11.5	2.58	AIS
228389	J122036.32+081904.2	0.2218	11.04	2.42	5.36	28.6	8.02	0.06	17.70	0.636	52	4.2	1.99	MIS
239110	J130434.51+271334.9	0.2201	11.10	4.48	8.41	44.5	7.55	0.03	17.33	0.630	52	4.9	2.28	MIS
232041	J132325.27+043707.6	0.1861	11.05*	1.98	4.59	20.1	9.69	0.08	17.53	0.511	61	20.7	...	...
232046	J133327.34+042244.8	0.1888	10.98	2.43	5.68	25.3	8.11	0.08	17.60	0.380	71	6.0	2.78	AIS
232055	J134211.36+053211.5	0.2031	10.82	2.36	5.45	26.3	7.90	0.08	17.75	0.540	59	9.1	2.31	AIS
232127	J135949.19+052731.8	0.2281	11.24	2.36	5.09	28.0	8.21	0.08	17.70	0.607	54	17.9	3.06	MIS
242091	J140522.72+052814.6	0.1954	11.03	3.12	6.42	29.7	7.91	0.07	17.23	0.458	65	17.5	2.63	MIS
242073	J140856.04+051616.3	0.1906	10.79	2.11	4.61	20.8	8.03	0.07	17.66	0.576	57	12.7	2.37	MIS
249558	J142151.16+100623.6	0.1938	11.29	3.33	6.54	30.0	8.13	0.08	17.00	0.790	39	16.8	2.62	MIS
242147	J142735.69+033434.2	0.2455	11.26	2.49	5.87	35.1	8.11	0.09	17.54	0.629	53	26.6	2.49	MIS
249559	J144518.88+025012.3	0.1906	11.17	2.62	6.21	28.0	8.23	0.11	17.28	0.773	40	15.6	3.01	MIS
249560	J144823.96+125551.9	0.1958	11.08	3.08	6.33	29.4	7.97	0.07	17.41	0.717	45	9.8	2.70	MIS
252580	J151337.28+041921.1	0.1754	10.78	3.60	7.94	32.6	7.64	0.13	17.57	0.441	66	6.1	2.38	MIS
252654	J153240.56+323428.8	0.2001	11.04	2.44	5.33	25.3	8.12	0.06	17.66	0.365	72	16.3	...	...
252641	J153400.67+001133.2	0.2036	11.02	2.24	4.84	23.5	8.15	0.21	17.49	0.547	59	6.2	2.07	MIS
262026	J160433.51+310900.0	0.2228	11.34	3.18	6.82	36.6	8.07	0.08	17.16	0.507	62	26.3	2.75	AIS
262029	J160938.00+312958.5	0.2188	11.30	2.87	6.44	33.8	8.15	0.09	17.20	0.608	54	20.5	2.84	AIS
262033	J162515.41+280530.3	0.1870	11.08	3.26	6.82	30.1	7.97	0.19	17.66	0.247	82	5.1	...	...
262015	J165940.12+344307.8	0.1982	10.83	2.69	5.59	26.3	7.83	0.06	17.54	0.591	55	7.7	2.15	MIS

*SDSS value was 12.37 (see text).

APPENDIX A: SDSS IMAGES AND ARECIBO HI SPECTRA

We present here SDSS postage stamp images and Arecibo HI-line spectra for the 39 HIGHz galaxies discussed in this work. These are organized as follows: Fig. A1 shows the 28 HI detections with quality flag Q = 1 in Table 2, and Fig. A2 and A3 show 5 galaxies with Q = 2 and 6 marginal detections with Q = 3, respectively. The objects in each of these figures are ordered by increasing AGC number (indicated on the top right corner of the SDSS image). The SDSS images show a 1 arcmin square field, *i.e.* only the central part of the region sampled by the Arecibo beam (the half power full width of the beam is $\sim$4′ at the frequencies of these observations). The HI spectra are always displayed over a velocity interval corresponding to the full 12.5 MHz bandwidth adopted for our observations. The HI-line profiles are calibrated, smoothed (to a velocity resolution between 27 and 41 km s^{-1}, as listed in Table 2), and baseline-subtracted. A red, dotted line indicates the heliocentric velocity corresponding to the optical redshift from SDSS. The shaded area and two vertical dashes show the part of the profile that was integrated to measure the HI flux and the peaks used for width measurement, respectively.

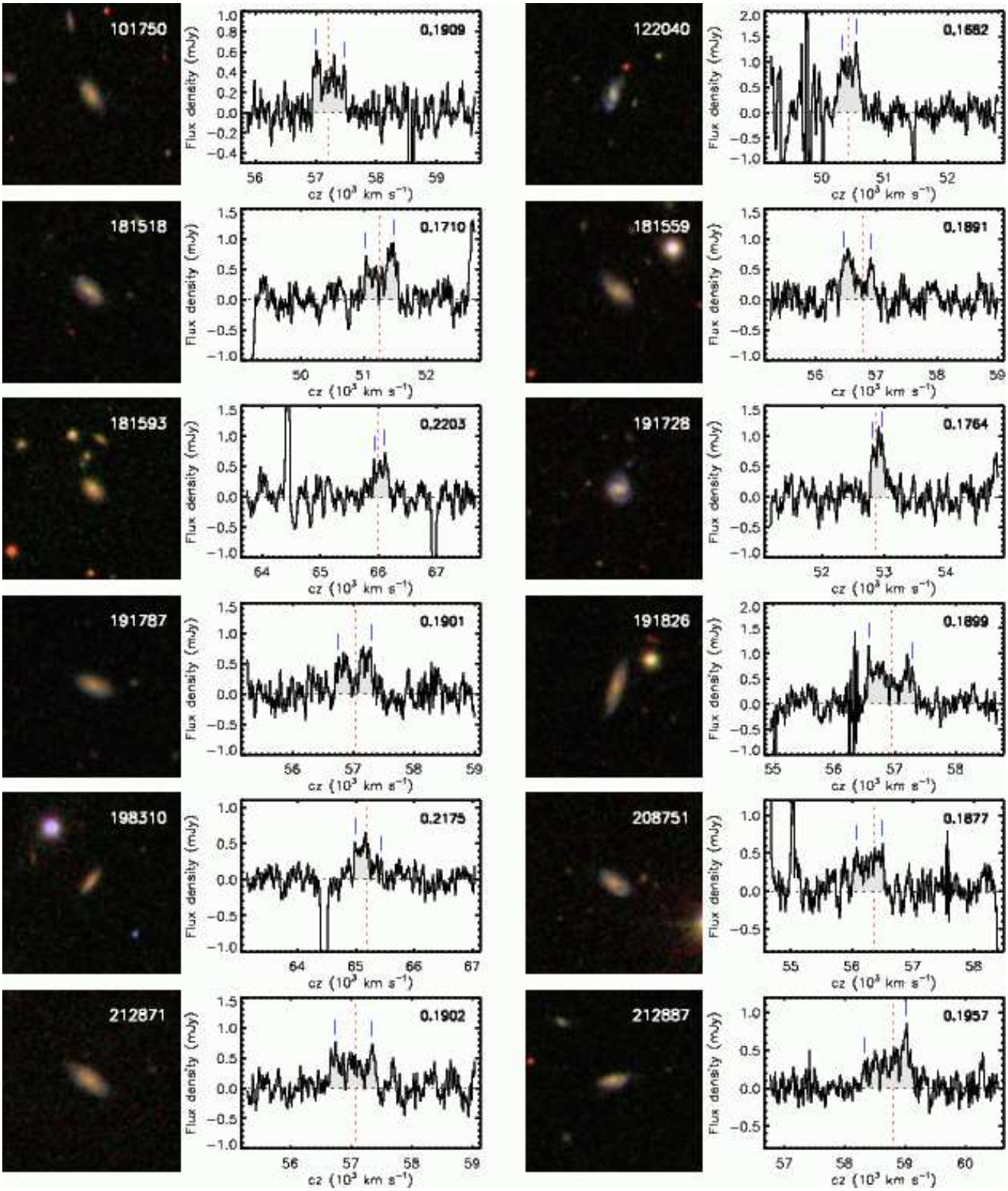

Figure A1. SDSS postage stamp images (1 arcmin square) and HI-line profiles of the best quality detections (code 1) presented in this work, ordered by increasing AGC number (indicated on each image). The HI spectra are calibrated, smoothed and baseline-subtracted. A dotted line and two dashes indicate the heliocentric velocity corresponding to the SDSS redshift and the two peaks used for width measurement, respectively. The redshift measured from the HI profile is indicated on the top right corner of the spectrum.

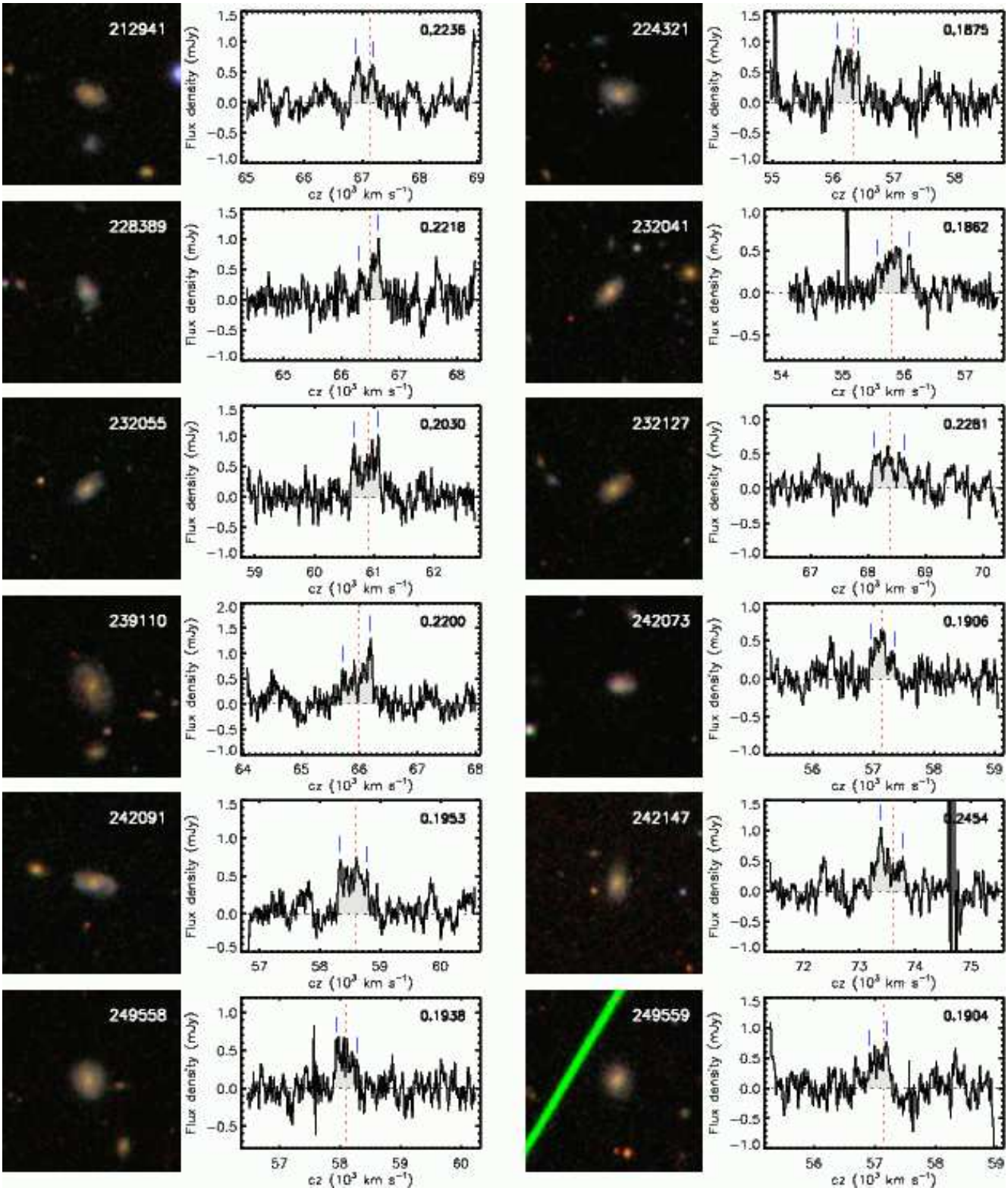

Figure A1. *continued*

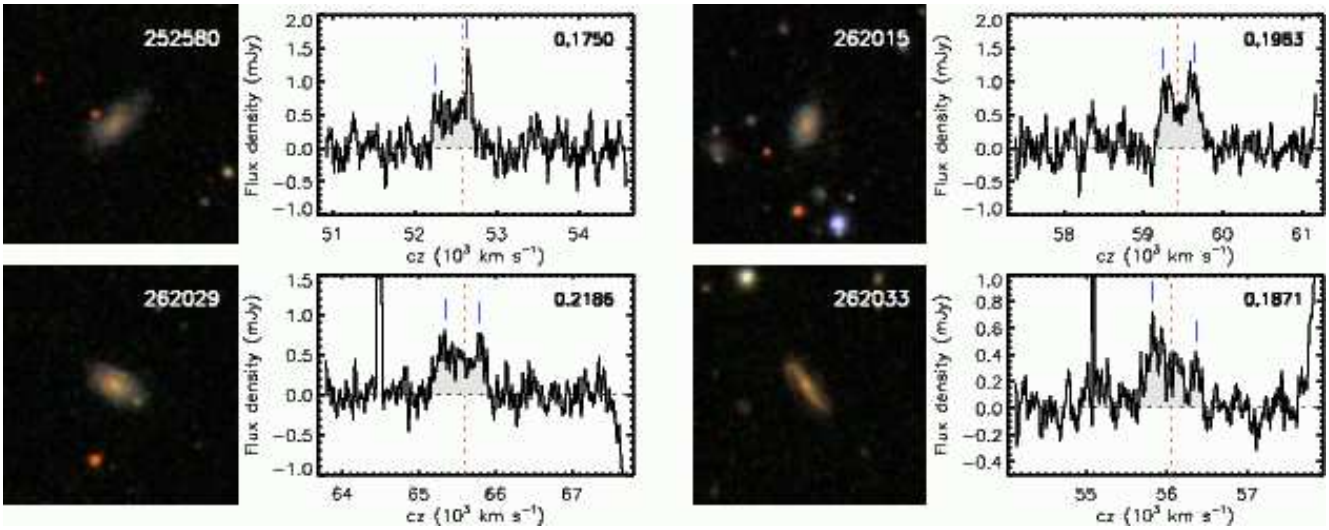

Figure A1. *continued*

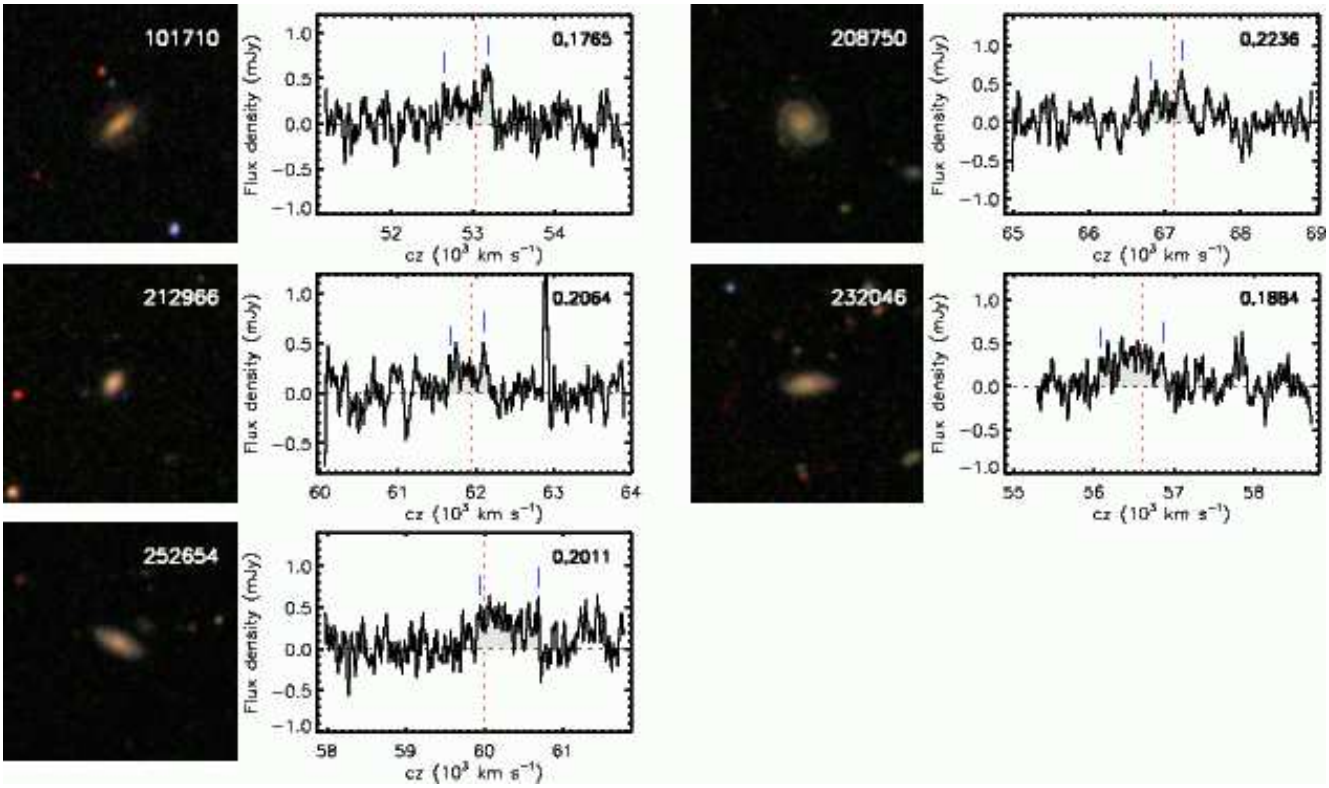

Figure A2. Same as Fig. A1 for lower signal-to-noise detections (code 2).

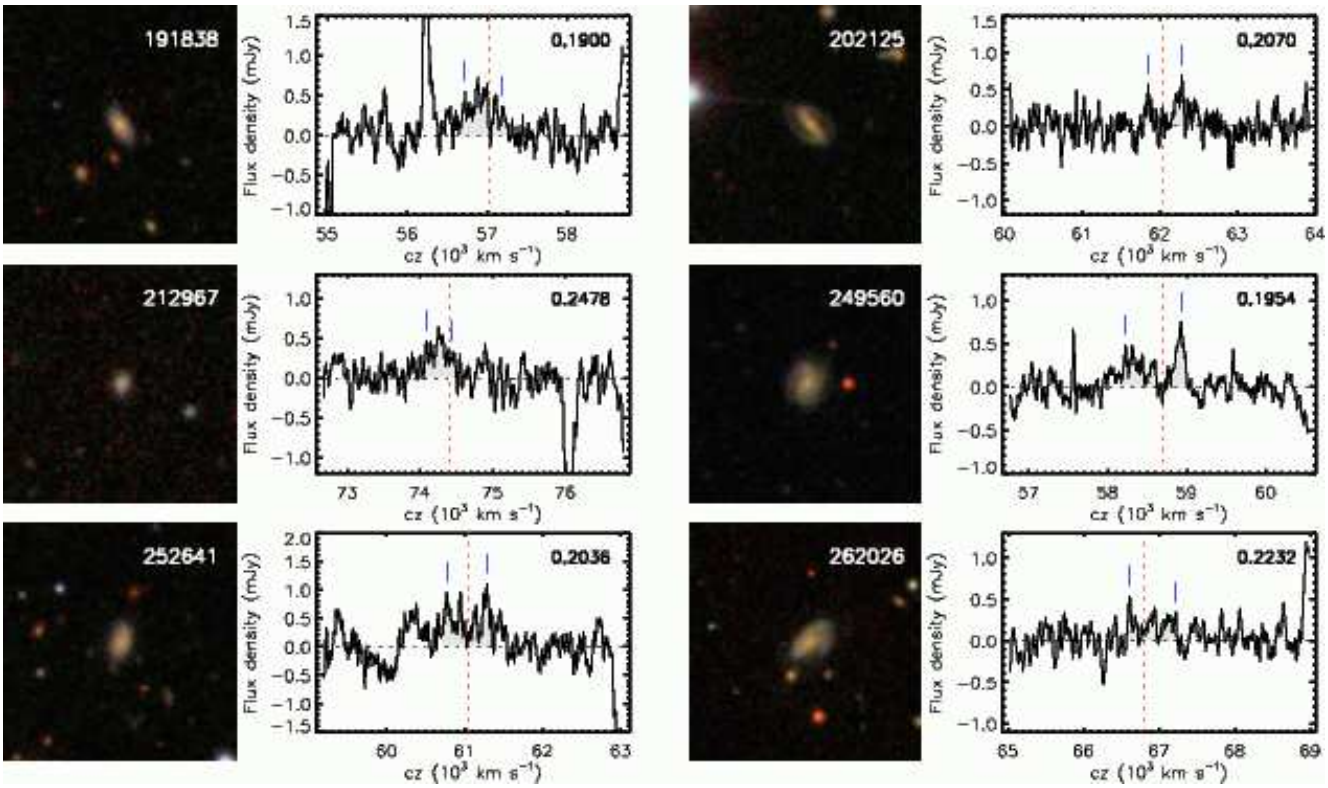

Figure A3. Same as Fig. A1 for marginal detections (code 3).